UNIVERSITY OF COPENHAGEN

MSc in Physics

Listening to Oscillatons

Gravitational Wave Scattering and Resonant Energy Transfer

Leart Sabani

Supervised by Vitor Cardoso and Thomas Spieksma

May 2026

Leart Sabani
Listening to Oscillatons
MSc in Physics, May 2026
Supervisors: Vitor Cardoso and Thomas Spieksma

University of Copenhagen
Faculty of Science
Niels Bohr Institute
Blegdamsvej 3B
2200 Copenhagen N

Acknowledgements

I would like to begin by sincerely thanking my two supervisors, Vitor Cardoso and Thomas Spieksma. I am eternally grateful for all the guidance and support they have given me throughout the past year while working on this project.

I am especially grateful to Thomas, not only for supervising me, but also for encouraging and motivating me to keep going when things did not go as planned or when I was having a difficult day. For that, I am deeply thankful.

I would also like to acknowledge that this thesis benefited from Mathematica notebooks provided by Richard Brito and Caio Macedo. Richard developed the Mathematica notebook used to derive the axial wave equations presented in this thesis, while Caio wrote the notebook used to solve the boson star background equations and compute their quasinormal modes.

Special thanks go to Lucía Vélez Tartajo for being a wonderful friend and for sharing every step of the thesis journey, the research, the writing, and everything in between. I would also like to thank the Strong Gravity group at the Center of Gravity, especially Rico, Lorena, Luka, Coner, Jaime, Juno, and Guangzi, remarkable people who made me feel that I truly belonged.

There are three people I will carry with me for the rest of my life: Amalie, Andreas, and Dina. I am not sure there are words enough for what they mean to me. I will never forget our late nights together, or our road trip across Europe, a journey that gave me some of my most cherished memories, and a rare escape from the stress and deadlines of student life. It is a genuine honour to call you my friends.

Finally, I want to thank my family and friends for their unwavering support. Above all, I am deeply grateful to my girlfriend, Julie Harder Gabrielsen, the most wonderful, spectacular person in my world, for standing by me through the hardest moments. I could not have done this without her.

Jeg kan godt,
og vil godt,
men uden jer,
betyder det ikke noget.

Abstract

Ultra-light scalar fields are well-motivated dark matter candidates that can form self-gravitating, coherent structures known as oscillatons. These arise as solutions of the Einstein–Klein–Gordon system for a real scalar field and exhibit intrinsic periodic time dependence.

In this thesis, we study the dynamics of axial gravitational perturbations on oscillaton backgrounds. The time-dependent nature of the spacetime leads to wave equations with periodic coefficients, making the system naturally suited for resonant energy exchange between the background and perturbations.

To construct these backgrounds, we numerically solve the Einstein–Klein–Gordon equations and generate a family of oscillaton configurations. This allows us to explore a wide range of spacetime geometries in a controlled way. Each configuration is characterised by standard global quantities such as the mass, radius, and compactness. However, the entire solution space can be parametrised by a single parameter, the central scalar-field amplitude, which uniquely determines the oscillaton profile.

We review the axial perturbation equation on oscillaton backgrounds and solve it numerically for different oscillaton configurations. Our results show that gravitational perturbations experience frequency-dependent energy exchange with the background. In particular, resonant amplification occurs when the perturbation frequency is tuned to integer multiples of the fundamental oscillation frequency of the oscillaton.

We find that the efficiency of this energy transfer increases with the central scalar-field amplitude, indicating a stronger coupling between perturbations and more compact oscillaton configurations. The results are consistent with a parametric resonance interpretation of wave propagation on a time-periodic gravitational background. This work demonstrates that oscillatons can significantly modify the propagation of gravitational perturbations through resonance effects, providing a first step toward understanding wave dynamics in time-dependent self-gravitating scalar-field spacetimes.

Contents

1 Introduction 1

2 Oscillatons 4

2.1 The Einstein-Klein-Gordon System . . . 4

2.2 Numerical Construction . . . 6

2.2.1 The origin of the mass loss . . . 8

3 Linear Perturbations of Oscillatons 11

3.1 Perturbative framework . . . 11

3.1.1 Spherical harmonic decomposition . . . 11

3.1.2 Linearized Einstein equations . . . 13

3.1.3 Oscillaton wave equation . . . 14

3.2 Parametric Resonance . . . 16

3.2.1 The Mathieu equation . . . 16

4 Numerical Framework 20

4.1 Spatial Finite Differencing . . . 20

4.2 Choosing initial data . . . 22

4.2.1 Gaussian profile . . . 22

4.2.2 Wavepacket . . . 23

4.3 Code validation . . . 23

4.3.1 Minkowski background . . . 23

4.3.2 Schwarzschild background . . . 25

5 Linear Response of Oscillatons 29

5.1 Gaussian initial data . . . 29

5.2 Wavepacket initial data . . . 33

5.2.1 The energy of the system . . . 33

5.3 Oscillatons as parametric drivers . . . 35

5.3.1 Small mass configurations . . . 36

5.3.2 Maximum mass oscillaton . . . 38

5.3.3 Energy gain at resonance . . . 41

5.4 Summary of results and discussion . . . 42

6 Conclusions and Outlook 43

7 Bibliography 45

A Matrix Pencil Method 50

B Declaration of using generative AI tools 52

Introduction

1

According to Isaac Newton, the dynamics of objects with mass follow one simple rule, $F = ma$: a particle of mass m accelerates in response to a force F. The simplicity of three letters and an equal sign is deceptive. In this one formula lies an entire branch of physics, which, with only modest assumptions about a system, can answer questions ranging from a box sliding down a sloped plane to the orbits of planets or the trajectories of comets. In this description, gravity is defined as the force exerted between massive objects.

In 1915, Albert Einstein revolutionized our understanding of gravity. In general relativity, gravity is no longer described as a force, but rather as a manifestation of the curvature of spacetime, encoded in the Einstein field equations $G_{\mu\nu} = 8\pi T_{\mu\nu}$. Ten coupled, non-linear partial differential equations condensed into a single compact relation: on one side, the geometry of spacetime; on the other, the matter and energy that shape it. Despite their concise form, the Einstein equations give rise to an extraordinarily rich phenomenology, including the bending of light around massive objects, the precession of Mercury's orbit, the expansion of the Universe, and the existence of compact objects such as neutron stars and black holes.

Almost immediately after Einstein published his theory, the German physicist and astronomer Karl Schwarzschild discovered an exact solution to these equations describing what would later become known as a black hole: a region of spacetime from which nothing, not even light, can escape. Together with neutron stars, black holes represent some of the most extreme manifestations of gravity in the Universe. Yet despite their seemingly exotic nature, black holes are remarkably simple objects. According to the no-hair theorems, an astrophysical black hole is fully characterized by at most three quantities: its mass, spin, and charge [1–6].

This underlying simplicity nevertheless gives rise to highly dynamical phenomena. As compact objects move through spacetime, they generate gravitational waves (GWs): ripples in the fabric of spacetime that propagate outward at the speed of light. Mathematically, gravitational waves can be understood as small perturbations of a background spacetime, allowing one to study the dynamics of the geometry without solving the full non-linear Einstein equations.

When two compact objects orbit one another, they emit gravitational radiation, gradually losing energy until they eventually merge. This process is commonly divided into three stages: the inspiral, where the orbit slowly shrinks; the merger, where the two objects coalesce; and the ringdown. In the case of black hole mergers, the ringdown phase is of particular interest because, according to linear perturbation theory, it is composed of discrete, exponentially damped oscillations known as quasinormal modes (QNMs). Crucially, these modes depend solely on the properties of the final black hole. By measuring them in gravitational-wave signals, we can infer the nature and characteristics of the compact object being observed, much like identifying a bell from its unique ring [7, 8].

On September 14, 2015, exactly one hundred years after Einstein's prediction of gravitational waves, the Laser Interferometer Gravitational-Wave Observatory recorded the first direct detection of such waves, produced by the merger of two stellar-mass black holes more than a billion light-years away [9]. This landmark observation marked the birth of gravitational-wave astronomy, opening an entirely new observational window onto the Universe. Since then, hundreds of gravitational-wave events have been detected [10–12].

The success of linear perturbation theory in black hole physics may also help us address other open problems in fundamental physics. One of such problems is the nature of dark matter, which makes up 27% of the total energy density of the Universe, while visible matter accounts for only 5%, as current data suggests [13]. Its existence is further supported by indirect evidence such as galactic rotation curves [14–20], gravitational lensing [21, 22], the large-scale structure of the Universe [23], and the cosmic microwave background [13]. Since dark matter does not interact with electromagnetic radiation, we cannot observe it through traditional means. In this context gravitational waves may provide a new window into its properties by revealing how it influences the signals we detect.

One compelling candidate is ultralight scalar fields, sometimes referred to as fuzzy or wave dark matter [24, 25]. In these models, dark matter is described by a bosonic scalar field with an extremely small mass, typically in the range $10^{-22}\ \mathrm{eV} \lesssim m \lesssim 10^{-20}\ \mathrm{eV}$ [26]. A striking feature of such light fields is that their wave-like nature becomes manifest on macroscopic, astrophysically relevant scales, a direct consequence of their extremely small mass and correspondingly large Compton wavelength. However, these models are subject to observational constraints. Using the Lyman-α forest, it has been shown that scalar field masses below $10^{-21}\ \mathrm{eV}$ are strongly disfavored [27, 28]. Even so, these models remain interesting from a phenomenological perspective, and of particular interest to this thesis is their ability to form self-gravitating structures.

Such self-gravitating structures have been studied extensively [29]. In particular, the case of a complex-valued scalar field minimally coupled to gravity gives rise to a family of solutions known as boson stars [29–34]. These compact objects are static and spherically symmetric, and have been studied both fully nonlinearly and perturbatively, showing that they exhibit behavior similar to black holes in the perturbative regime, for example, admitting a discrete set of complex quasinormal frequencies [35].

A closely related set of objects arises when the scalar field is taken to be real-valued. Numerical studies have shown that, given generic spherically symmetric initial data, such a scalar field relaxes into a quasi-stable, spatially localized, oscillating object known as an oscillaton [36]. These objects are not perfectly stable: owing to their oscillatory nature, they slowly radiate scalar field away and lose mass over time. However, this process occurs so slowly that on astrophysical timescales [37, 38], the configuration can be well approximated as strictly periodic, and it is this approximation of the full dynamical evolution that we refer to as an oscillaton throughout this thesis.

The existence of oscillatons raises a natural and important question: how do gravitational waves interact with these objects? If ultralight scalar dark matter condenses into oscillaton-like structures, then gravitational waves passing through or scattering off such structures could carry imprints of the encounter.

Understanding this interaction is therefore not only of theoretical interest but also has direct observational implications for gravitational wave detectors such as LIGO, or future detectors such as LISA [39] (Laser Interferometer Space Antenna) or the Einstein Telescope [40].

A key feature that distinguishes oscillatons from other compact objects such as boson stars or black holes is the explicit time dependence of the background spacetime. Unlike a black hole, whose spacetime is stationary and admits a clean notion of QNMs, or a boson star, whose scalar field produces a stationary background, an oscillaton breathes, its metric and scalar field oscillate periodically in time. This raises the question of whether such a time-dependent background can leave a frequency-dependent imprint on passing gravitational waves, and whether it opens the door to resonant phenomena well known from classical mechanics. This thesis takes a first step in addressing these questions.

This thesis is organized as follows. In Chap. 2, we review the background theory of oscillatons and their solutions. In Chap. 3, we briefly review linear perturbation theory in general relativity, derive the wave equations governing gravitational perturbations on oscillaton backgrounds, and review the theory of parametric resonance. In Chap. 4, we outline the numerical scheme used to solve the wave equation derived in Chap. 3, and validate the procedure by testing the code on well-understood backgrounds. Chapter 5 studies the response of gravitational perturbations interacting with an oscillaton.

Oscillatons

2

In this chapter, we review the construction of the oscillaton background. We begin by defining the field equations and our choice of coordinate system, followed by a discussion on the stability of these objects and the numerical methods used to solve for their periodic configurations. In this thesis, we use the mostly plus metric signature $(-,+,+,+)$ and work in units where $G=\hbar=c=1$.

2.1 The Einstein-Klein-Gordon System

Oscillatons consist of real-valued scalar fields minimally coupled to gravity. They arise as solutions to the Einstein-Klein-Gordon equations, obtained from the Einstein-Hilbert action supplemented by a massive real-valued scalar field term [36]

$$S=\int \mathrm{d}^4x\sqrt{-g}\left(\frac{R}{16\pi}-\frac{1}{2}\left(\nabla_\mu\Phi\nabla^\mu\Phi+\mu^2\Phi^2\right)\right), \tag{2.1}$$

where R is the Ricci scalar, ∇_μ the covariant derivative, and $\mu=m_\mathrm{B}/\hbar$ the scalar field mass parameter. Varying the action with respect to the metric and the scalar field, respectively, yields the Einstein field equations and the Klein-Gordon equation,

$$R_{\mu\nu}-\frac{1}{2}Rg_{\mu\nu}=8\pi T_{\mu\nu}\,,\qquad \nabla_\mu\nabla^\mu\Phi-\mu^2\Phi=0\,, \tag{2.2}$$

where the stress-energy tensor $T_{\mu\nu}$ takes the standard scalar field form

$$T_{\mu\nu}=\nabla_\mu\Phi\nabla_\nu\Phi-\frac{1}{2}g_{\mu\nu}(\nabla_\alpha\Phi\nabla^\alpha\Phi+\mu^2\Phi^2)\,. \tag{2.3}$$

The geometric content is encoded in the Ricci tensor $R_{\mu\nu}$, which is constructed from the Christoffel symbols $\Gamma^\mu_{\nu\rho}$ through

$$R_{\mu\nu}=\partial_\alpha\Gamma^\alpha_{\mu\nu}-\partial_\nu\Gamma^\alpha_{\mu\alpha}+\Gamma^\alpha_{\alpha\beta}\Gamma^\beta_{\mu\nu}-\Gamma^\alpha_{\mu\beta}\Gamma^\beta_{\alpha\nu}\,, \tag{2.4}$$

with the Christoffel symbols themselves determined by the metric via

$$\Gamma^\mu_{\nu\rho}=\frac{1}{2}g^{\mu\sigma}\left(\partial_\nu g_{\sigma\rho}+\partial_\rho g_{\sigma\nu}-\partial_\sigma g_{\nu\rho}\right)\,. \tag{2.5}$$

We assume that the scalar field is spherically symmetric such that $\Phi \equiv \Phi(t, r)$, and that the background spacetime also becomes spherically symmetric, with the line element being written as

$$ds^2 = -\frac{B(t,r)}{C(t,r)}\mathrm{d}t^2 + B(t,r)\mathrm{d}r^2 + r^2\mathrm{d}\theta^2 + r^2\sin^2\theta\mathrm{d}\phi^2\,. \tag{2.6}$$

Similar to Ref. [41], we write the g_{tt} component as B/C for numerical convenience. Rescaling the scalar field by $1/\sqrt{4\pi}$, the equations of motion (EOM) for the system become:

$$\frac{\partial_r B}{B} = \frac{r}{2}\left[(\partial_t\Phi)^2 C + (\partial_r\Phi)^2 + B\mu^2\Phi^2\right] + \frac{1-B}{r}\,, \tag{2.7}$$

$$\frac{\partial_r C}{C} = \frac{2}{r}\left[1 + B\left(\frac{(r\mu\Phi)^2}{2} - 1\right)\right]\,, \tag{2.8}$$

$$\left(C\partial_t^2 - \partial_r^2\right)\Phi = \left(\frac{2}{r} - \frac{\partial_r C}{2C}\right)\partial_r\Phi - \frac{\partial_t C}{2}\partial_t\Phi - B\mu^2\Phi\,. \tag{2.9}$$

Instead of dynamically evolving the scalar field to obtain fully time-dependent oscillaton solutions [36, 38, 42, 43], we approximate the long-lived, quasi-periodic phase by strictly periodic configurations. This is a well-justified approximation, as the decay time of oscillatons can vastly exceed the age of the universe. For a maximum-mass oscillaton, the half-life of its mass is approximately [44, 45]

$$t_{1/2} \sim 10^{46}\ \text{years}\left(\frac{10^{-21}\,\text{eV}}{m_B c^2}\right)\,. \tag{2.10}$$

2.2 Numerical Construction

As noted above, oscillatons are not strictly periodic but slowly decay over time. During the long-lived quasiperiodic phase, however, this decay is negligible, and we may treat the background as strictly periodic. We therefore expand the fields $B(t,r)$, $C(t,r)$, and $\Phi(t,r)$ in a Fourier-like harmonic series [43],

$$B(t,r) = \sum_{n=0}^{N} b_n(r)\cos(2\omega n t)\,, \tag{2.11}$$

$$C(t,r) = \sum_{n=0}^{N} c_n(r)\cos(2\omega n t)\,, \tag{2.12}$$

$$\Phi(t,r) = \sum_{n=0}^{N} \phi_{n+1}(r)\cos(2\omega n t + \omega t)\,. \tag{2.13}$$

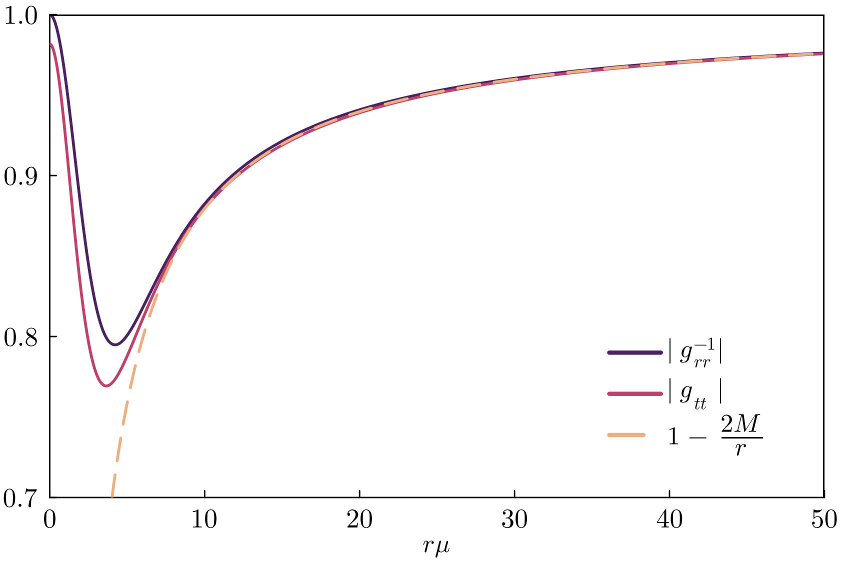

Figure 2.1: A solution of Eqs. (2.7) for the metric functions $B(t,r)$ and $C(t,r)$ with $N=1$, plotted as $g_{tt} = B/C$ and $g_{rr}^{-1} = 1/B$. The solution has characteristic frequency $\omega \approx 0.862\mu$, mass $M \approx 0.603/\mu$ and radius $R \approx 7.36/\mu$. The plot is showing the metric components evaluated at $t=0$.

Substituting these into Eqs. (2.7) and matching frequency components results in $3(N+1)$ coupled non-linear ordinary differential equations (ODEs). We treat the system as a boundary value problem. At the origin ($r=0$), regularity requires $b_0 = 1$ and $b_{n>0} = 0$, while the scalar field modes must satisfy $\partial_r \phi_n = 0$. At spatial infinity ($r \to \infty$), asymptotic flatness requires $b_0 = c_0 = 1$ and all higher modes to vanish. To solve this numerically, we use a *shooting method*: we fix the central scalar field value $\phi_1(0)$ and integrate outward, tuning the eigenvalues $\{c_0, c_1, \ldots, \omega\}|_{r=0}$ until the conditions at a large numerical radius $r_{\max}$ are satisfied. Specifically, we ensure the solution smoothly approaches the Schwarzschild background by requiring:

$$\left(c_0 - b_0^2\right)|_{r=r_{\max}} = 0\,. \tag{2.14}$$

A representative solution for the metric functions is shown in Fig. 2.1. The figure also shows that our background indeed approaches Schwarzschild as r increases. To get a better sense of the physical properties of the oscillaton, we will use a few diagnostics to characterize the oscillaton. Because of the asymptotically Schwarzschild behavior of our oscillaton backgrounds, we may define the mass of these configurations as the Schwarzschild mass, such that, in units of $\mu = 1$, we have

$$M \equiv \lim_{r\to\infty} \frac{r}{2}\left(1 - \frac{1}{b_0(r)}\right)\,. \tag{2.15}$$

Not including the higher order terms of the B metric function, corresponds to averaging out the higher order terms in time. We do not have access to infinity, so we truncate this limit to some large radii $r_{\max}$, in which the background is approximately Schwarzschild. So we evaluate the mass at this large radius

$$M \approx \frac{r_{\max}}{2}\left(1 - \frac{1}{b_0(r_{\max})}\right)\,. \tag{2.16}$$

The radius of the oscillaton is a bit more tricky to define since there are no hard boundaries for which we can call “inside the oscillaton” and “outside the oscillaton”. Similar to previous works, we set the radius to be the radius at which 98% of the total oscillaton mass is contained in. This is an arbitrary choice, and in the existing literature on oscillatons, multiple choices have been made, including the percentiles $95\%, 98\%$ and 99%. This does not change the physics, only the relative comparison between physical observables and the oscillaton. From these two parameters, we may also define a compactness parameter denoted by

$$\mathcal{C} = \frac{M}{R}\,. \tag{2.17}$$

This gives us a measure of how tightly localized the oscillaton is, representing the intensity of the spacetime curvature it generates. For example, the compactness of a Schwarzschild black hole would be $\mathcal{C}_{\text{Sch}} = 0.5$.

To understand how oscillaton configurations change as the central scalar field value is varied, we begin by constructing solutions with a relatively small central value of the scalar field, typically around $\phi_1(r = 0) = 0.05$. Once such a solution is obtained, additional configurations with larger central scalar field values can be computed efficiently by using the previously obtained solution as an initial guess for the numerical solver. This procedure allows us to generate a sequence of oscillaton solutions by gradually increasing the central amplitude of the scalar field (see Fig. 2.2).

We observe that the space of oscillaton configurations contains a maximum-mass configuration at a central scalar field value of approximately $\phi_1(r=0) \approx 0.334$. This configuration has a mass $M \approx 0.603/\mu$, a radius $R \approx 7.36/\mu$, and a characteristic frequency $\omega \approx 0.862\mu$, which is in perfect agreement with previous work [41–43].

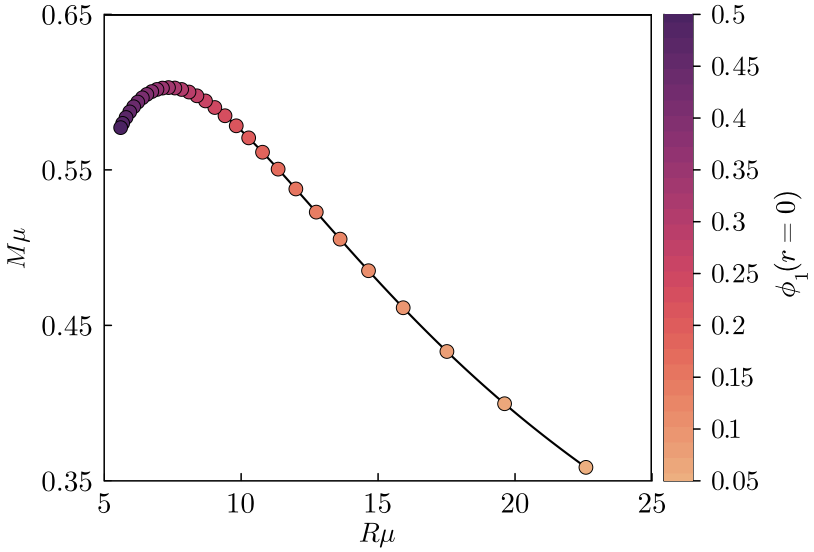

Figure 2.2: Mass and radius of different oscillaton configurations as a function of the central value of the first order scalar field ϕ_1. Every 100th solution is plotted with a dot, to not clutter the plot. The plot shows a maximum oscillaton mass at $M \approx 0.603/\mu$, with a corresponding radius of $R \approx 7.36/\mu$.

2.2.1 The origin of the mass loss

To understand the physical origin of this mass loss within the strictly periodic approximation, we examine the behavior of the scalar field expansion at large distances. In the far region, where the metric is approximately Minkowski, the Klein-Gordon equation (2.7) reduces to

$$-\partial_t^2\Phi + \partial_r^2\Phi + \frac{2}{r}\partial_r\Phi - \mu^2\Phi = 0\,. \tag{2.18}$$

Substituting the harmonic expansion (2.13) and defining $\phi_n(r) = f_n(r)/r$, we obtain the radial equation for each mode:

$$\partial_r^2 f_n = (\mu^2 - n^2\omega^2) f_n\,, \tag{2.19}$$

which has the general solution

$$f_n(r) = c_1 e^{-r\sqrt{\mu^2-n^2\omega^2}} + c_2 e^{r\sqrt{\mu^2-n^2\omega^2}}\,. \tag{2.20}$$

From this solution, we can consider two scenarios: $n\omega < \mu$, the solution decays exponentially at large radii, or written out explicitly

$$f_n(r) = c_n e^{-r\lambda_n}\,, \quad \lambda_n = \sqrt{\mu^2 - n^2\omega^2}\,. \tag{2.21}$$

However, for sufficiently high harmonics such that $n\omega > \mu$, the square root becomes imaginary. The solution is then written

$$f_n(r) = c_n \cos(\lambda_n r + \alpha_n)\,, \quad \lambda_n = \sqrt{n^2\omega^2 - \mu^2}\,. \tag{2.22}$$

These modes turn out to be radiative, and we may see this if we write out the full time dependence explicitly, such that

$$\Phi_n \sim \frac{c_n}{r}\cos(\lambda_n r - n\omega t + \alpha_n)\,, \quad \lambda_n = \sqrt{n^2\omega^2 - \mu^2}\,, \tag{2.23}$$

which describes an outgoing spherical wave with radial wavenumber λ_n and temporal frequency $n\omega$. To confirm that these modes carry energy to infinity, we compute the radial energy flux using the stress-energy tensor of the scalar field. In the far region, the tr-component is

$$T^{tr} = -\partial_t\Phi\,\partial_r\Phi\,. \tag{2.24}$$

Taking derivatives of Eq. (2.23) and retaining only the leading terms at large r, we get

$$\partial_t\Phi_n = \frac{n\omega c_n}{r}\sin(\lambda_n r - n\omega t + \alpha_n)\,, \tag{2.25}$$

$$\partial_r\Phi_n = -\frac{\lambda_n c_n}{r}\sin(\lambda_n r - n\omega t + \alpha_n) + \mathcal{O}(r^{-2})\,, \tag{2.26}$$

so that

$$T^{tr} = \frac{n\omega\lambda_n c_n^2}{r^2}\sin^2(\lambda_n r - n\omega t + \alpha_n)\,. \tag{2.27}$$

The energy carried by the radiative modes, through a sphere of radius r is then calculated as

$$\begin{aligned}\mathcal{P}_n &= \int_\Omega r^2 T^{tr}\,d\Omega \\ &= 4\pi n\omega\lambda_n c_n^2 \sin^2(\lambda_n r - n\omega t + \alpha_n)\,.\end{aligned} \tag{2.28}$$

Time-averaging over one oscillation period, $\langle\sin^2\rangle = 1/2$, the total power radiated through a sphere of radius r is

$$\langle\mathcal{P}_n\rangle = 2\pi n\omega\lambda_n c_n^2\,. \tag{2.29}$$

This is the key result: the radiated power $\langle \mathcal{P}_n \rangle$ is independent of r, confirming that the energy flux does not diminish with distance and that these modes carry energy all the way to spatial infinity. In contrast, for the bound modes with $n\omega < \mu$, the field falls off as $e^{-\lambda_n r}/r$, so that $T^{tr} \sim e^{-2\lambda_n r}/r^2$ and the integrated flux vanishes exponentially, so no energy escapes to infinity. This means that if we want to consider a scalar field configuration that is localized, and not purely radiative, then at least $\omega < \mu$.

The existence of a threshold $n\omega > \mu$ means that only harmonics above a critical mode number contribute to the radiation, while the fundamental mode remains bound. Since the amplitudes c_n of the higher harmonics are generically small, the total radiated power is extremely weak, which explains why oscillatons are so long-lived despite being strictly speaking unstable [46]. As noted in Ref. [45], these oscillatory modes represent non-localized solutions, and their amplitudes set the overall decay rate of the configuration.

Linear Perturbations of Oscillatons

3

In this chapter, we review the derivation of the equations governing linear gravitational perturbations on oscillaton backgrounds. Our aim is to obtain a wave equation describing the evolution of these perturbations in a time-dependent spacetime.

The analysis follows the standard framework of linear perturbation theory in curved spacetime, closely paralleling the treatment of perturbations around spherically symmetric backgrounds such as black holes. However, the explicit time dependence of the oscillaton geometry leads to important differences, which are reflected in the structure of the resulting wave equation.

In addition, we review the theory of parametric resonance, focusing on the Mathieu equation as a prototypical example of a system with time-periodic coefficients. This will provide useful intuition for understanding the behavior of the perturbation equations derived in this chapter.

3.1 Perturbative framework

In this section, we review the formalism required to describe linear perturbations of the oscillaton spacetime. Exploiting the spherical symmetry of the background, we decompose the perturbations into tensor spherical harmonics, allowing us to separate the angular dependence and reduce the problem to a set of equations for each multipole. We then derive the linearized Einstein equations and obtain the wave equation governing the perturbations.

3.1.1 Spherical harmonic decomposition

We consider linear perturbations of the oscillaton background introduced in Chap. 2. The spacetime metric can be written as a perturbative expansion around this background,

$$g_{\mu\nu} = g^{\mathrm{b}}_{\mu\nu} + \epsilon h_{\mu\nu} \,, \tag{3.1}$$

where $|\epsilon| \ll 1$, and all equations are retained to first order in ϵ. Here, $g^{\mathrm{b}}_{\mu\nu}$ denotes the previously defined spherically symmetric, time-dependent background metric (see Eq. (2.6)), and $h_{\mu\nu}$ represents small metric perturbations.

Since the background metric is spherically symmetric, we can choose coordinates that allow us to decompose any rank-2 tensor field as [47]

$$X_{\mu\nu} = \begin{pmatrix} X_{AB} & X_{Aa} \\ X_{aA} & X_{ab} \end{pmatrix} \,, \tag{3.2}$$

where we split the coordinates $x^\mu = (t, r, \theta, \varphi)$, such that uppercase Latin letters refer to $x^A = (t, r)$ and lowercase letters refer to $x^a = (\theta, \varphi)$.

The metric perturbation $h_{\mu\nu}$ is itself a rank-2 tensor field defined on the background spacetime. It can therefore be decomposed in terms of tensor spherical harmonics (with an implicit sum over ℓ and m, and using the notation in Ref. [47])

$$\begin{aligned} h_{AB}(t,r,\theta,\varphi) &= \bar{h}_{AB\,\ell m}(t,r)\, Y^{\ell m}(\theta,\varphi)\,, && (3.3)\\ h_{Aa}(t,r,\theta,\varphi) &= \bar{h}^{\text{polar}}_{A\,\ell m}(t,r)\, Y^{\ell m}_a(\theta,\varphi) + \bar{h}^{\text{axial}}_{A\,\ell m}(t,r)\, S^{\ell m}_a(\theta,\varphi)\,, && (3.4)\\ h_{ab}(t,r,\theta,\varphi) &= r^2\left[K_{\ell m}(t,r)\,\gamma_{ab}Y^{\ell m}(\theta,\varphi) + G_{\ell m}(t,r)\, Z^{\ell m}_{ab}(\theta,\varphi)\right] \\ &\quad + 2\bar{h}_{\ell m}(t,r)\, S^{\ell m}_{ab}(\theta,\varphi)\,. && (3.5) \end{aligned}$$

Here, $\gamma_{ab} = \mathrm{diag}(1, \sin^2\theta)$ denotes the metric on the unit two-sphere. Let D_a be the covariant derivative compatible with γ_{ab}, such that

$$\gamma^{ab} D_a D_b Y^{\ell m} = -\ell(\ell+1) Y^{\ell m}\,, \tag{3.6}$$

where $Y^{\ell m}$ are the usual scalar spherical harmonics.

The tensor spherical harmonics used in the expansion above are generalizations of these scalar harmonics and are defined as

$$\begin{aligned} Y^{\ell m}_a &= D_a Y^{\ell m}\,, && (3.7)\\ S^{\ell m}_a &= -\sqrt{\det\gamma}\,\epsilon_{ab} D^b Y^{\ell m}\,, && (3.8)\\ Z^{\ell m}_{ab} &= D_a D_b Y^{\ell m} + \frac{\ell(\ell+1)}{2}\gamma_{ab} Y^{\ell m}\,, && (3.9)\\ S^{\ell m}_{ab} &= \frac{1}{2}\left(D_a S^{\ell m}_b + D_b S^{\ell m}_a\right)\,, && (3.10) \end{aligned}$$

where ϵ_{ab} is the Levi-Civita tensor on the two-sphere, antisymmetric in its indices ($\epsilon_{ab} = -\epsilon_{ba}$).

Note that while scalar harmonics are defined for all $\ell \geq 0$, the vector harmonics are nonzero only for $\ell \geq 1$, and the tensor harmonics are nonzero only for $\ell \geq 2$. The tensor harmonics can also be split into two groups, one which transform oddly under a parity transformation $(\theta, \varphi) \to (\pi - \theta, \varphi + \pi)$, and one that transforms evenly.

Odd parity (Axial)

The axial sector is spanned by $S^{\ell m}_a$ and $S^{\ell m}_{ab}$, which transform under parity as

$$\begin{aligned} S^{\ell m}_a(\pi-\theta, \varphi+\pi) &= (-1)^{\ell+1} S^{\ell m}_a(\theta,\varphi)\,, && (3.11)\\ S^{\ell m}_{ab}(\pi-\theta, \varphi+\pi) &= (-1)^{\ell+1} S^{\ell m}_{ab}(\theta,\varphi)\,. && (3.12) \end{aligned}$$

Even parity (Polar)

The polar sector is spanned by $Y^{\ell m}$, $Y_a^{\ell m}$ and $Z_{ab}^{\ell m}$, which transform under parity as

$$Y^{\ell m}(\pi-\theta,\varphi+\pi)=(-1)^{\ell}Y^{\ell m}(\theta,\varphi)\,, \tag{3.13}$$

$$Y_a^{\ell m}(\pi-\theta,\varphi+\pi)=(-1)^{\ell}Y_a^{\ell m}(\theta,\varphi)\,, \tag{3.14}$$

$$Z_{ab}^{\ell m}(\pi-\theta,\varphi+\pi)=(-1)^{\ell}Z_{ab}^{\ell m}(\theta,\varphi)\,. \tag{3.15}$$

In the Regge-Wheeler gauge [48], we set the components $\bar{h}^{\text{polar}}_{A\,\ell m}=G_{\ell m}=\bar{h}_{\ell m}=0$. The metric perturbation in this gauge then become

$$h_{\mu\nu}=\begin{pmatrix}\bar{h}_{AB\,\ell m}Y^{\ell m} & \bar{h}^{\text{axial}}_{A\,\ell m}S_a^{\ell m}\\ \bar{h}^{\text{axial}}_{A\,\ell m}S_a^{\ell m} & r^2K_{\ell m}\gamma_{ab}Y^{\ell m}\end{pmatrix} \tag{3.16}$$

$$=h^{\text{polar}}_{\mu\nu}+h^{\text{axial}}_{\mu\nu}\,. \tag{3.17}$$

3.1.2 Linearized Einstein equations

Having established the decomposition of the metric perturbations in terms of tensor spherical harmonics, we now turn to the equations governing their dynamics. We know that the background metric $g^{\text{b}}_{\mu\nu}$, together with the scalar field Φ^{b}, solves the Einstein field equations

$$G_{\mu\nu}\left[g^{\text{b}}\right]=8\pi T_{\mu\nu}\left[g^{\text{b}},\Phi^{\text{b}}\right]\,. \tag{3.18}$$

Consider now a first order linear perturbation to the scalar field $\phi(x^{\mu})$, such that the full scalar field takes the form

$$\Phi(x^{\mu})=\Phi^{\text{b}}(t,r)+\epsilon\,\phi(x^{\mu})\,, \tag{3.19}$$

where, like when we perturbed the metric in Eq. (3.1), ϵ is a perturbative bookkeeping parameter. We may do a separation of variables, and write the scalar field perturbation in terms of spherical harmonics

$$\Phi(x^{\mu})=\Phi^{\text{b}}(t,r)+\epsilon\,\phi(t,r)Y^{\ell m}(\theta,\varphi)\,. \tag{3.20}$$

Now plugging in the full metric and scalar field, and expand to first order in ϵ, we get [49]

$$G^{\text{b}}_{\mu\nu}+\epsilon\Delta G_{\mu\nu}=8\pi(T^{\text{b}}_{\mu\nu}+\epsilon\Delta T_{\mu\nu})\,, \tag{3.21}$$

which if we insert that $G^{\text{b}}_{\mu\nu}=8\pi T^{\text{b}}_{\mu\nu}$, we get

$$\Delta G_{\mu\nu}=8\pi\Delta T_{\mu\nu}\,. \tag{3.22}$$

For convenience lets define the tensor $\Delta\mathcal{E}_{\mu\nu} \equiv \Delta G_{\mu\nu} - 8\pi\Delta T_{\mu\nu}$. Now decomposing this tensor using tensor harmonics, as described in Sec. 3.1.1, we get (with an implicit sum over ℓ and m, and following notation from Ref. [47]):

$$\begin{aligned}
\Delta\mathcal{E}_{AB} &= A^{(A+B)}_{\ell m}(t,r)Y^{\ell m}\,, && (3.23)\\
\Delta\mathcal{E}_{Aa} &= \alpha^{(A)}_{\ell m}(t,r)Y^{\ell m}_a + \beta^{(A)}_{\ell m}(t,r)S^{\ell m}_a\,, && (3.24)\\
\Delta\mathcal{E}_{ab} &= A^{(3)}_{\ell m}(t,r)\,r^2\gamma_{ab}Y^{\ell m} + s_{\ell m}(t,r)Z^{\ell m}_{ab} + t_{\ell m}(t,r)S^{\ell m}_{ab}\,. && (3.25)
\end{aligned}$$

Since the polar and axial sectors have opposite parity, they decouple, and the linearized equations, $\Delta\mathcal{E}_{\mu\nu} = 0$, split into two independent sets. The polar sector requires

$$A^{(A)}_{\ell m} = 0\,, \quad A^{(3)}_{\ell m} = 0\,, \quad \alpha^{(A)}_{\ell m} = 0\,, \quad s_{\ell m} = 0\,, \tag{3.26}$$

in which $A^{(A)}_{\ell m}$,$\alpha^{(A)}_{\ell m}$ (with $A = 0,1$), $A^{(3)}_{\ell m}$ and $s_{\ell m}$ only depend on the polar components of the metric perturbations $h^{\rm polar}_{\mu\nu}$. While the axial sector is determined by

$$\beta^{(A)}_{\ell m} = 0\,, \quad t_{\ell m} = 0\,, \tag{3.27}$$

in which $\beta^{(A)}_{\ell m}$ (with $A = 0,1$) and $t_{\ell m}$ only depend on the axial components of the metric perturbations $h^{\rm axial}_{\mu\nu}$ [48].

3.1.3 Oscillaton wave equation

In this work, we focus on the axial sector, governed by Eqs. (3.27). A key simplification arises from the fact that scalar field perturbations do not contribute to this sector. We can explicitly see this if we write out $\Delta T_{\mu\nu}$

$$\begin{aligned}
\Delta T_{\mu\nu} = {}& \partial_\mu\Phi^{\rm b}\partial_\nu(\phi Y^{\ell m}) + \partial_\mu(\phi Y^{\ell m})\partial_\nu\Phi^{\rm b}\\
&- g^{\rm b}_{\mu\nu}\left[\partial_\alpha\Phi\partial^\alpha(\phi Y^{\ell m}) + \mu^2\Phi\phi Y^{\ell m}\right]\\
&+ \frac{1}{2}g^{\rm b}_{\mu\nu}\partial_\alpha\Phi^{\rm b}\partial^\alpha\Phi^{\rm b} - \frac{1}{2}h_{\mu\nu}\left[\partial_\alpha\Phi^{\rm b}\partial^\alpha\Phi^{\rm b} + \mu^2\Phi^{\rm b}\right]\,.
\end{aligned} \tag{3.28}$$

If we only look at the terms involving the scalar field perturbations, we see that they are either proportional to $Y^{\ell m}$ or $\partial_\mu Y^{\ell m}$, which vanishes for $\mu = 0,1$ and equals $Y^{\ell m}_a$ for $\mu = 2,3$. Both $Y^{\ell m}$ and $Y^{\ell m}_a$ are even-parity harmonics, and since $\partial_a\Phi^{\rm b} = 0$, no odd-parity harmonics $S^{\ell m}_a$ or $S^{\ell m}_{ab}$ can appear. The remaining terms in $\Delta T_{\mu\nu}$ are proportional to $h_{\mu\nu}$, which carries the same parity as the metric perturbation itself, so axial metric perturbations source only axial equations, and polar metric perturbations source only polar equations.

Plugging in the oscillaton background solution, and expanding $\beta^{(0)}_{\ell m} = 0$, we obtain

$$\begin{aligned}
0 =& \left[\frac{(\ell-1)(\ell+1)}{2r^2} + \frac{2}{2r^2 B} + \frac{B\partial_r C - 2C\partial_r B}{2rCB^2}\right] h^{\text{axial}}_{0\,\ell m} \\
&- \left[\frac{B\partial_r C - 2C\partial_r B}{4CB^2}\right] \partial_r h^{\text{axial}}_{0\,\ell m} - \frac{\partial_r^2 h^{\text{axial}}_{0\,\ell m}}{2B} \\
&+ \left[\frac{1}{rB} + \frac{B\partial_r C - 2C\partial_r B}{4CB^2}\right] \partial_t h^{\text{axial}}_{1\,\ell m} + \frac{\partial_t \partial_r h^{\text{axial}}_{1\,\ell m}}{2B}\,,
\end{aligned} \tag{3.29}$$

while $\beta^{(1)}_{\ell m} = 0$ gives

$$\begin{aligned}
0 =& \frac{(\ell-1)(\ell+2)}{2r^2} h^{\text{axial}}_{1\,\ell m} + \left[\frac{B\partial_t C - 2C\partial_t B}{4B^2}\right] \partial_t h^{\text{axial}}_{1\,\ell m} + \frac{C\partial_t^2 h^{\text{axial}}_{1\,\ell m}}{2B} \\
&+ \left[\frac{B\partial_t C - 2C\partial_t B}{2rB^2}\right] h^{\text{axial}}_{0\,\ell m} - \left[\frac{B\partial_t C - 2C\partial_t B}{4B^2}\right] h^{\text{axial}}_{0\,\ell m} \\
&+ \frac{C\partial_t h^{\text{axial}}_{0\,\ell m}}{rB} - \frac{C\partial_t \partial_r h^{\text{axial}}_{0\,\ell m}}{2B}\,.
\end{aligned} \tag{3.30}$$

To simplify this system, it is useful to introduce a master variable that captures the physical content of the axial perturbations. Following a construction analogous to the Cunningham-Price-Moncrief master function [50], we define

$$\psi^{\text{axial}}_{\ell m} \equiv -\frac{2r\sqrt{C}}{(\ell-1)(\ell+2)B}\left(\frac{2h^{\text{axial}}_{0\,\ell m}}{r} - \partial_r h^{\text{axial}}_{0\,\ell m} - \partial_t h^{\text{axial}}_{1\,\ell m}\right)\,. \tag{3.31}$$

Solving for the metric perturbations in terms of this master variable, one finds

$$h^{\text{axial}}_{0\,\ell m} = \frac{1}{2\sqrt{C}}\left(\psi^{\text{axial}}_{\ell m} + r\partial_r \psi^{\text{axial}}_{\ell m}\right)\,, \tag{3.32}$$

$$h^{\text{axial}}_{1\,\ell m} = \frac{r}{2}\sqrt{C}\,\partial_r \psi^{\text{axial}}_{\ell m}\,. \tag{3.33}$$

Substituting these expressions into the remaining equation $t_{\ell m} = 0$, we obtain a single wave equation for the master variable,

$$\left[-\partial_t^2 + \frac{1}{\sqrt{C}}\partial_r\left(\frac{1}{\sqrt{C}}\partial_r\right) - \frac{\partial_t C}{2C}\partial_t - V\right]\psi^{\text{axial}}_{\ell m} = 0\,, \tag{3.34}$$

with effective potential

$$V = \frac{B}{C}\left[\frac{(\ell-1)(\ell+2)}{r^2} + \frac{2}{r^2 B} + \frac{\partial_r C}{2rBC}\right]\,. \tag{3.35}$$

The time-dependent background introduces an additional first-order time derivative term proportional to $\partial_t C$, which acts as a driving or damping term. This term can be removed by a simple redefinition of the master function. Consider the rescaling

$$\psi^{\text{axial}}_{\ell m}(t,r) = e^{\int \alpha(t,r)\,dt}\,\chi_{\ell m}(t,r)\,, \tag{3.36}$$

and choose $\alpha(t,r)$ such that the first-order time derivative in Eq. (3.34) vanishes. This yields

$$\alpha = -\frac{1}{4}\partial_t \ln C \,, \tag{3.37}$$

from which we obtain

$$\chi_{\ell m}(t,r) = C^{1/4}(t,r)\, \psi^{\text{axial}}_{\ell m}(t,r) \,. \tag{3.38}$$

In terms of $\chi_{\ell m}$, the wave equation takes the simpler form

$$\left[-\partial_t^2 + \partial_r\left(\frac{1}{C}\partial_r\right) - \tilde{V}\right]\chi_{\ell m} = 0 \,, \tag{3.39}$$

where $\tilde{V}$ differs from V by terms involving derivatives of $C(t,r)$. While the two formulations are mathematically equivalent, this form provides a clearer physical interpretation in terms of wave propagation in a time-dependent effective medium.

3.2 Parametric Resonance

In the previous section, we derived the linearized equations governing perturbations on the oscillaton background. Due to the explicit time dependence of the background spacetime, the resulting perturbation equations contain time-periodic coefficients.

Such systems are known to exhibit *parametric resonance*, where small perturbations can undergo exponential growth driven by periodic modulation of the background. This phenomenon is typically associated with the appearance of instability bands and plays an important role in a wide range of physical systems.

To develop intuition for these effects, we briefly review the theory of parametric resonance in a simpler setting. In the following subsection, we introduce the Mathieu equation, which captures the essential features of linear systems with periodic coefficients.

3.2.1 The Mathieu equation

The simplest prototype of a linear system with periodic coefficients is the harmonic oscillator with a time-dependent frequency. Despite its simplicity, this model captures the essential features of parametric resonance, including instability bands and exponentially growing solutions.

We begin by considering the simple harmonic oscillator, whose equation of motion is

$$\partial_t^2 x(t) = -\omega_0^2 x(t) \,. \tag{3.40}$$

This system admits the well-known solution

$$x(t) = Ae^{i\omega_0 t} + Be^{-i\omega_0 t}\,, \tag{3.41}$$

where $A, B \in \mathbb{C}$, describing oscillatory motion with constant frequency ω_0.

A natural generalization is obtained by allowing the oscillator frequency to vary in time, thereby modeling the effect of an external periodically varying background. The equation of motion then becomes

$$\partial_t^2 x(t) = -\omega^2(t)\, x(t)\,. \tag{3.42}$$

In this case, the dynamics can differ qualitatively from the simple harmonic oscillator, particularly if the time dependence introduces new frequency scales into the problem. Assuming a periodic modulation with period $T = 2\pi/\Omega$, and further restricting to small deviations from the constant frequency case, we consider

$$\partial_t^2 x(t) = -\Big[\omega_0^2 + \epsilon\cos(\Omega t)\Big]\, x(t)\,, \tag{3.43}$$

where $|\epsilon| \ll 1$. This describes an oscillator whose effective restoring force is modulated in time, and provides a simple setting in which parametric resonance can arise.

To bring this equation into a more standard form, we introduce the rescaled time variable $\tau = \Omega t/2$, which yields

$$\partial_\tau^2 x(\tau) = -\left[\frac{4\omega_0^2}{\Omega^2} + \frac{4\epsilon}{\Omega^2}\cos(2\tau)\right] x(\tau)\,. \tag{3.44}$$

Defining the dimensionless parameters

$$a = \frac{4\omega_0^2}{\Omega^2}\,, \qquad q = -\frac{2\epsilon}{\Omega^2}\,, \tag{3.45}$$

the equation can be written in the form

$$\partial_\tau^2 x(\tau) = -\left[a - 2q\cos(2\tau)\right] x(\tau)\,, \tag{3.46}$$

which is known as the Mathieu equation [51, 52]. The presence of periodic coefficients leads to qualitatively new behavior compared to the ordinary harmonic oscillator. In particular, solutions are not generically bounded, and small perturbations can undergo exponential growth for certain parameter values. This phenomenon is known as parametric resonance.

The structure of the solutions can be understood using Floquet theory [52], which states that solutions to equations of this type can be written as

$$x(\tau) = e^{\mu\tau} P(\tau)\,, \tag{3.47}$$

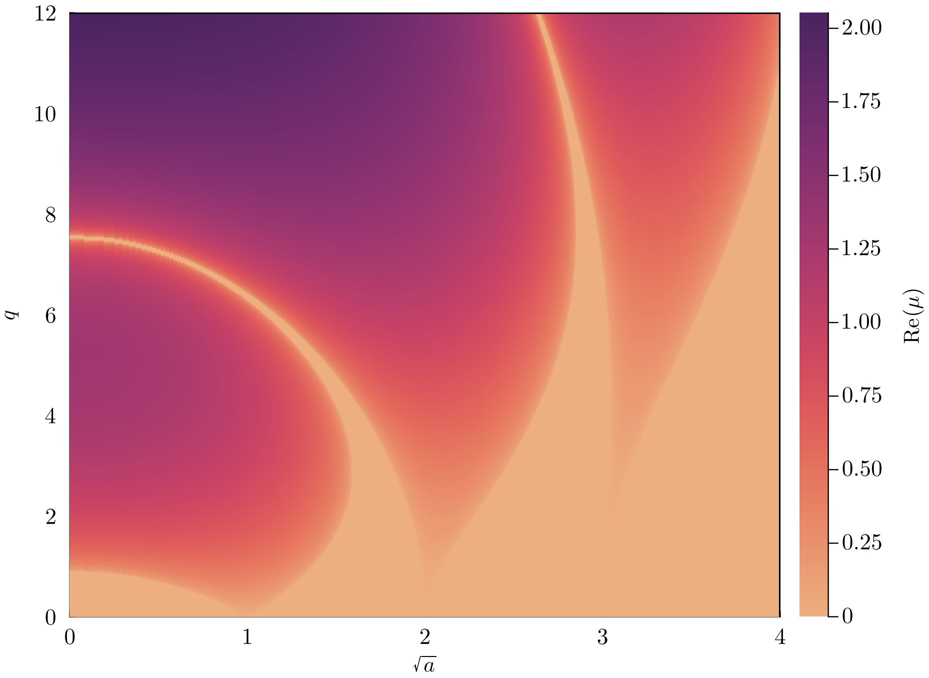

Figure 3.1: Heatmap showing the unstable regions of the solutions to the Mathtieu equation (3.46). In the yellow regions of the $\{\sqrt{a}, q\}$ plane, all the solutions are stable, meaning that $\mathrm{Re}(\mu) = 0$, while in the purple regions solutions become unstable, with $\mathrm{Re}(\mu) > 0$.

where μ is known as the Floquet exponent, and $P(\tau)$ is a periodic function, with same period as the system. In the case of the Mathieu system the period is such that $P(\tau + \pi) = P(\tau)$. Since $P(\tau)$ is periodic, we may expand it in a Fourier series

$$P(\tau) = \sum_{n=-\infty}^{\infty} c_n e^{2in\tau}\,, \tag{3.48}$$

where each of the c_n's are the mode coefficients. The solution $x(\tau)$ is set to be unstable if $\mathrm{Re}\,(\mu) > 0$ [52]. Substituting the full expression of $x(\tau)$ into Eq. (3.46), and collecting terms with the same exponential $e^{(\mu+2in)\tau}$ gives the recursion relation

$$[(\mu + 2in)^2 + a]c_n - q(c_{n+1} + c_{n-1}) = 0\,. \tag{3.49}$$

Given a set of variables $\{a, q\}$, we can solve this by treating it as an infinite matrix eigenvalue problem for μ [53], where $\mathrm{Re}(\mu) > 0$ signals an unstable solution (see Fig. 3.1).

For small values of ϵ, it can be shown that parametric resonance only happens when the natural frequency ω_0 is close to integer multiples of half the driving frequency,

$$\omega_0 \approx \frac{n\Omega}{2}\,, \qquad n = 1, 2, \ldots \tag{3.50}$$

Within these bands, the Floquet exponent acquires a nonzero real part, $\mathrm{Re}(\mu) \neq 0$, and the solutions grow or decay exponentially. Outside these regions, μ is purely imaginary and the motion remains bounded. This instability structure is a generic feature of systems with time-periodic parameters and will play an important role in understanding the dynamics of perturbations on the oscillaton background.

Numerical Framework

4

In this chapter, we present the numerical framework used to evolve the perturbation equations introduced in the previous sections. The central question we wish to address is whether the explicit time dependence of the oscillaton background can lead to resonant amplification and cumulative energy gain. Answering this requires a stable and accurate time-domain evolution scheme capable of resolving the oscillatory behavior of the system across a range of oscillaton configurations. We achieve this by discretizing the governing wave equation in space using high-order finite-difference methods, combined with explicit time-integration techniques.

We begin by outlining the spatial discretization and how the wave equation is cast into a first-order-in-time system suitable for numerical evolution. We then describe the choice of initial data used to generate physically relevant signals suited for probing the scattering properties of the background. Finally, we validate the numerical implementation by applying it to well-understood test cases, including Minkowski and Schwarzschild backgrounds, where analytical and semi-analytical results are available for comparison.

4.1 Spatial Finite Differencing

As established in Sec. 3.1.3, the axial perturbations are governed by two mathematically equivalent wave equations, related by the rescaling $\chi_{\ell m} = C^{1/4}\psi^{\text{axial}}_{\ell m}$. The choice of which to evolve numerically is a matter of convenience; in this thesis we work directly with the unrescaled equation for $\psi^{\text{axial}}_{\ell m}$, Eq. (3.34). To solve a wave equation, we discretize space with grid spacing Δr and evaluate the wave function at uniformly spaced points. To ensure numerical stability and convergence, we choose the time-step size according to the CFL condition, which places an upper bound on the time spacing. The CFL condition requires that the time step satisfy

$$\Delta t < \frac{\Delta r}{c_{\max}}\,, \tag{4.1}$$

where $c_{\max}$ is the maximum propagation speed of the wave equation. From Eq. (3.34), we see that the propagation speed is $c_{\max} = 1/\sqrt{C}$, which is always less than or equal to unity. We therefore choose $\Delta t = 0.5\,\Delta r$, which comfortably satisfies the CFL condition. The discretized wavefunction is denoted by

$$\psi^n_i \equiv \psi^{\text{Axial}}_{\ell m}(n\Delta t, i\Delta r)\,. \tag{4.2}$$

where i indexes the spatial grid points and n indexes the time steps. Spatial derivatives are approximated using fourth-order finite differences:

$$\partial_r \psi_i^n \approx \frac{\psi_{i-2}^n - 8\psi_{i-1}^n + 8\psi_{i+1}^n - \psi_{i+2}^n}{12\Delta r}\,, \tag{4.3}$$

$$\partial_r^2 \psi_i^n \approx \frac{-\psi_{i-2}^n + 16\psi_{i-1}^n - 30\psi_i^n + 16\psi_{i+1}^n - \psi_{i+2}^n}{12\Delta r^2}\,. \tag{4.4}$$

We transform the second-order wave equation (Eq. (3.34)) into a first-order system by defining the state vector

$$U_i^n = \begin{pmatrix} \psi_i^n \\ \partial_t \psi_i^n \end{pmatrix}\,. \tag{4.5}$$

With this definition, the derivative in time of the state vector is calculated

$$\partial_t U_i^n = \mathbf{F}_i^n U_i^n\,, \tag{4.6}$$

where the matrix $\mathbf{F}_i^n$ is defined as

$$\mathbf{F}_i^n \equiv \frac{1}{C_i^n} \begin{pmatrix} 0 & C_i^n \\ \partial_r^2 - \frac{\partial_r C_i^n}{2C_i^n}\partial_r & -\frac{1}{2}\partial_t C_i^n \end{pmatrix}\,. \tag{4.7}$$

Integrating the wave equation will be done using a fourth-order Runga-Kutta scheme, in which a single step in the time direction is computed using four intermediate steps in the following way

$$k_{1,i}^n = \mathbf{F}_i^n U_i^n\,, \tag{4.8}$$

$$k_{2,i}^n = \mathbf{F}_i^{n+\frac{1}{2}} \left(U_i^n + \frac{\Delta t}{2} k_{1,i}^n \right)\,, \tag{4.9}$$

$$k_{3,i}^n = \mathbf{F}_i^{n+\frac{1}{2}} \left(U_i^n + \frac{\Delta t}{2} k_{2,i}^n \right)\,, \tag{4.10}$$

$$k_{4,i}^n = \mathbf{F}_i^{n+1} \left(U_i^n + \Delta t\, k_{3,i}^n \right) \tag{4.11}$$

$$U_i^{n+1} = U_i^n + \frac{\Delta t}{6}(k_{1,i}^n + 2k_{2,i}^n + 2k_{3,i}^n + k_{4,i}^n)\,. \tag{4.12}$$

Given some initial state vector at some time t, we may use this scheme to get a new state vector at some later time $t + \Delta t$. To reduce memory usage, only the newest state vector and a few selected spatial indices are stored, allowing extraction of a time-domain signal at a chosen spatial location r, typically far from the central object. This will give us a signal in the form of an array like

$$\Psi = [\psi_I^0, \psi_I^1, \ldots, \psi_I^{N-1}, \psi_I^N]\,, \tag{4.13}$$

where I is the spatial index we are saving, and N is the maximum number of time steps. Since both the finite differencing and the time integration are fourth-order accurate, we expect the overall scheme to also exhibit fourth-order convergence. This can be verified by defining a reference grid with N_r^{n} radial grid points and comparing it with finer ($N_r^{\mathrm{f}} = 2\,N_r^{\mathrm{n}}$) and coarser ($N_r^{\mathrm{c}} = \frac{1}{2}N_r^{\mathrm{n}}$) grids.

To quantify the convergence, we evaluate the convergence order at each time step using the extracted signals $\Psi_{\mathrm{n}}, \Psi_{\mathrm{c}}$ and Ψ_{f}, corresponding to the reference, coarse, and fine grids, respectively. For a given time step k, we calculate the convergence order as

$$\log_2\left|\frac{\Psi_{\mathrm{c}}^k - \Psi_{\mathrm{n}}^k}{\Psi_{\mathrm{n}}^k - \Psi_{\mathrm{f}}^k}\right| . \tag{4.14}$$

This is verified explicitly for a number of test cases in Sec. 4.3.

4.2 Choosing initial data

In order to solve the wave equation in the time domain, it is necessary to specify initial conditions for the perturbation field. These initial data determine both the spatial profile of the perturbation and its subsequent propagation.

In this work, we consider localized initial configurations that allow us to probe how perturbations evolve on the background spacetime. By appropriately choosing the initial profile and its time derivative, we can control properties such as localization, frequency content, and direction of propagation.

4.2.1 Gaussian profile

A natural and straightforward choice of initial data is a Gaussian profile:

$$\psi(t=0,r) = \psi_0 e^{-\frac{(r-r_0)^2}{2\sigma^2}}, \tag{4.15}$$

where $\psi(t,r)$ is the perturbation field, ψ_0 is the amplitude of the Gaussian, r_0 is its center, and σ is the width. The initial time derivative $\partial_t\psi(t=0,r)$ can be chosen to control the direction of wave propagation. Introducing null coordinates:

$$u = t - r_* \quad \Rightarrow \quad \partial_u = \frac{1}{2}(\partial_t - \partial_*), \tag{4.16}$$

$$v = t + r_* \quad \Rightarrow \quad \partial_v = \frac{1}{2}(\partial_t + \partial_*), \tag{4.17}$$

where r_* is the tortoise coordinate, and $\partial_* \equiv \frac{\partial}{\partial r_*}$. In this thesis we will work with two kinds of initial conditions,

- **Stationary Gaussian:** $\partial_t\psi = 0$ corresponds to a combination of left- and right-moving components.

- **Ingoing Gaussian:** $\partial_u\psi = 0$ gives $\partial_t\psi = \partial_*\psi$.

This explicitly determines the initial velocity profile of the Gaussian and ensures the intended propagation direction.

4.2.2 Wavepacket

A natural generalization of the Gaussian profile is a *wavepacket*, obtained by modulating the Gaussian with a plane-wave factor

$$\psi(t=0,r) = \psi_0\, e^{-\frac{(r-r_0)^2}{2\sigma^2} + i\omega_d(r-r_0)}\,, \tag{4.18}$$

where ω_d is the central wavenumber of the packet. Unlike the Gaussian initial data, the wavepacket carries a non-zero average momentum.

To understand the spectral content of the initial data, we compute its Fourier transform. Although ω_d sets the central wavenumber, the finite width of the Gaussian envelope broadens the spectrum and introduces contributions from neighbouring frequencies. The one-sided Fourier transform is

$$\tilde{\psi}(k) = \int_0^\infty dr\, \psi(r) e^{-ikr}\,, \tag{4.19}$$

$$= \psi_0 e^{-ikr_0} e^{-\frac{\sigma^2}{2}(k-\omega_\mathrm{d})^2} \sqrt{\frac{\pi}{2}} \left[1 + \mathrm{erf}\left(\frac{r_0 - i\sigma^2(k-\omega_\mathrm{d})}{\sigma\sqrt{2}}\right)\right]. \tag{4.20}$$

In the limit $r_0 \gg \sigma$, this reduces to

$$\tilde{\psi}(k) \sim e^{-\frac{\sigma^2}{2}(k-\omega_\mathrm{d})^2}\,, \tag{4.21}$$

demonstrating that the Fourier transform of a Gaussian wavepacket is itself Gaussian in frequency space, centered at $k = \omega_\mathrm{d}$ with width proportional to σ^{-1}.

4.3 Code validation

To validate the numerical procedure, we start by testing our scheme on well understood spacetime backgrounds, such as flat Minkowski and the Schwarzschild black hole background. This will give us a good benchmark for the accuracy of the implementation of the scheme.

4.3.1 Minkowski background

We begin by validating the numerical implementation on a Minkowski background, for which the metric functions are constant and may be chosen as $B = C = 1$. In this case, Eq. (3.34) reduces to

$$\partial_t^2 \psi = \partial_r^2 \psi - \frac{\ell(\ell+1)}{r^2}\psi\,. \tag{4.22}$$

We consider Gaussian initial data corresponding to both stationary and ingoing configurations. Since Minkowski spacetime does not contain an effective trapping region or horizon, the evolved signal is expected to consist only of the direct propagation of the initial pulse.

Figure 4.1 shows the waveform extracted at $r = 200M$ for stationary initial data and $\ell = 2$. The left panel displays the time-domain signal at three different spatial resolutions. The waveform exhibits the characteristic double-peaked structure associated with the prompt response [54], corresponding to the ingoing and outgoing parts of the initial perturbation propagating through the extraction radius.

The top right panel shows the differences between successive resolutions. Rescaling the fine, normal difference by the expected fourth-order factor produces excellent overlap with the normal, coarse difference, demonstrating that the implementation achieves the expected fourth-order convergence. At late times (approximately $t > 250M$), the differences approach machine precision, after which the convergence estimate becomes unreliable due to numerical roundoff error.

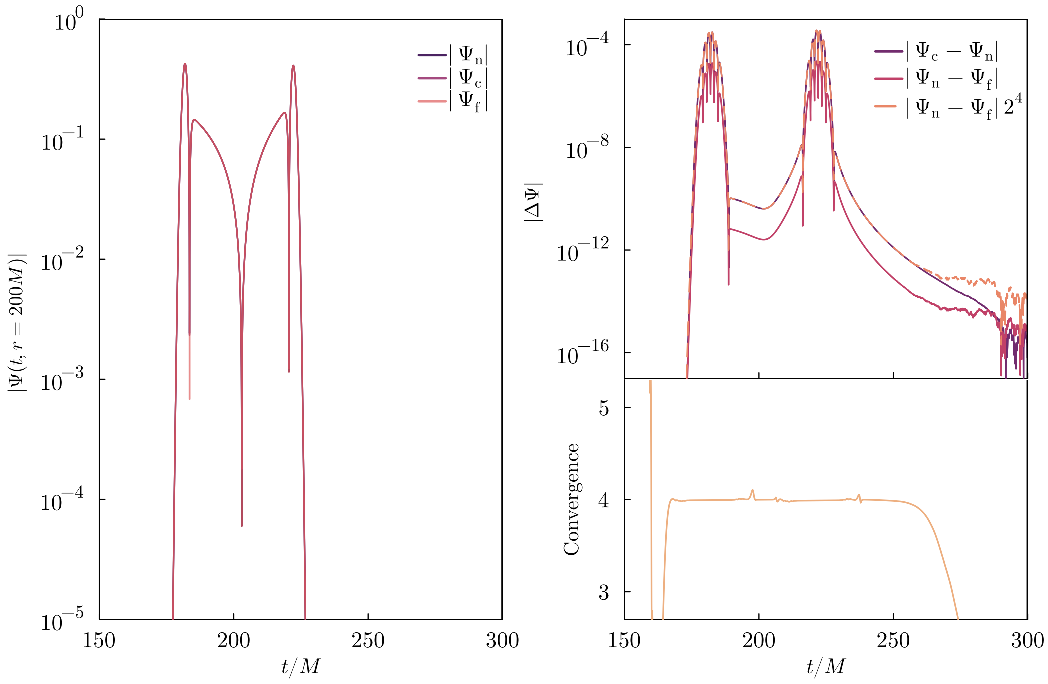

Figure 4.1: Time-domain waveform $\Psi(t, r = 200M)$ evolved on a Minkowski background with $\ell = 2$ from stationary Gaussian initial data (**left**). Relative differences between successive resolutions together with the rescaled fine–normal difference assuming fourth-order convergence (**top right**). Measured convergence order, as a function of time (**bottom right**). The simulations are performed at resolutions $N_r^{\rm c} = 1.5 \times 10^4$, $N_r^{\rm n} = 3 \times 10^4$, and $N_r^{\rm f} = 6 \times 10^4$. The overlap between the rescaled and unscaled differences demonstrates fourth-order convergence. At late times, the convergence estimate becomes unreliable as the differences approach machine precision. The same convergence behaviour is observed for ingoing initial data.

4.3.2 Schwarzschild background

To further test our scheme, we apply the code to a Schwarzschild background. Linear perturbations on a Schwarzschild black-hole background are well understood, making this an ideal benchmark for our numerical approach before turning to time-dependent backgrounds, such as oscillatons. Axial gravitational perturbations in the Schwarzschild background are described by the Regge–Wheeler (RW) equation [48]. We can get the RW equation by inserting

$$B = \left(1 - \frac{2M}{r}\right)^{-1} \quad \text{and} \quad C = B^2 \,, \tag{4.23}$$

into Eq. (3.34), which gives us

$$-\frac{\partial^2}{\partial t^2}\psi + \frac{\partial^2}{\partial r_*^2}\psi - \left(1 - \frac{2M}{r}\right)\left(\frac{\ell(\ell+1)}{r^2} - \frac{6M}{r^3}\right)\psi = 0 \,, \tag{4.24}$$

where the tortoise coordinate r_* is related to the radial coordinate r by

$$\frac{\mathrm{d}r_*}{\mathrm{d}r} = \left(1 - \frac{2M}{r}\right)^{-1} . \tag{4.25}$$

It is convenient to formulate and discretise the evolution equation in r_* rather than r. This choice maps the exterior domain $r \in (2M, \infty)$ to $r_* \in (-\infty, \infty)$ and yields a more uniform resolution of both the near-horizon and asymptotic regions.

Solving Eq. (4.25) gives

$$r_*(r) = r + 2M \ln\left(\frac{r}{2M} - 1\right) , \tag{4.26}$$

which can be inverted numerically to obtain $r = r(r_*)$. The potential is then expressed as $V = V(r_*)$ and evaluated directly on the computational grid. As in the flat-spacetime case, we assess the convergence properties of our numerical implementation by evolving the Regge–Wheeler equation on three different spatial resolutions and comparing the resulting solutions to estimate the convergence order. We consider two types of initial data, given by Gaussian profiles corresponding to stationary and ingoing waves.

Figures 4.2 demonstrate that the numerical scheme maintains fourth-order convergence for stationary initial data on a Schwarzschild background, providing confidence in the accuracy and reliability of the time evolution. Similar tests using ingoing initial data yield comparably good results.

Furthermore, we validate our code by comparing the numerical waveforms to the theoretically expected signal structure [7, 55]. The time-domain response consists of a superposition of exponentially damped quasinormal modes together with a late-time power-law tail.

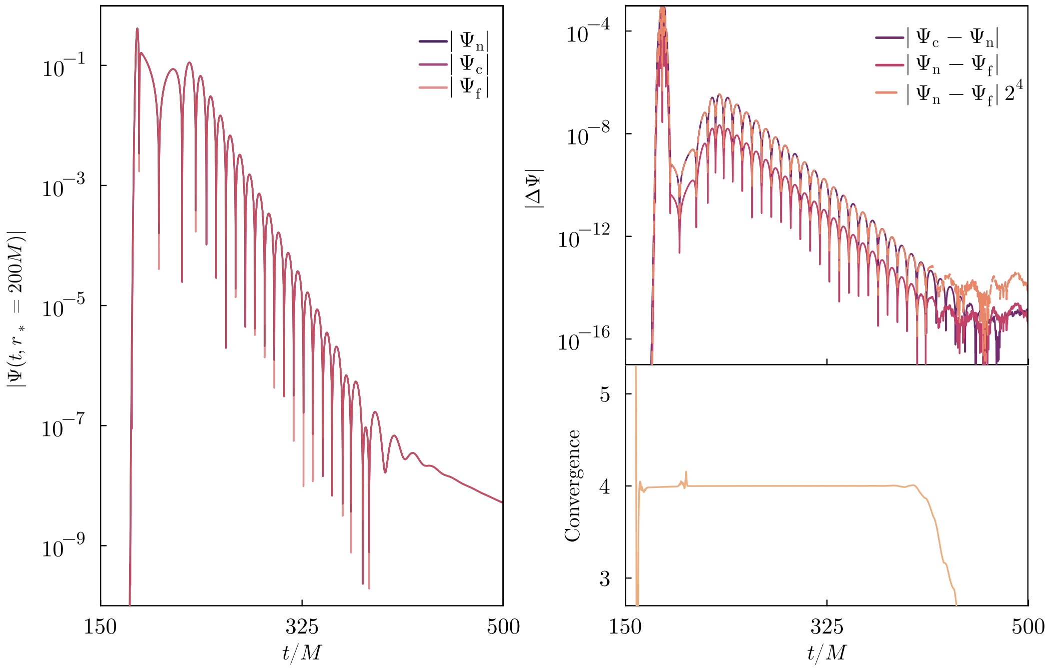

Figure 4.2: Time-domain waveform $\Psi(t, r_* = 200M)$ evolved on a Schwarzschild background with $\ell = 2$, using the same setup and resolutions as in Fig. 4.1 (**left**). In contrast to the flat-space case, curvature-induced scattering is present. Relative differences between successive resolutions together with the rescaled fine–normal difference assuming fourth-order convergence (**top right**). Measured convergence order as a function of time (**bottom right**). Fourth-order convergence is observed. At late times, the estimate becomes unreliable as differences approach machine precision, as in Fig. 4.1. The same behaviour holds for ingoing initial data.

To extract the quasinormal-mode frequencies from the signal, we employ the Matrix Pencil Method [56] (MPM) (see App. A). In this method, the waveform is modeled within a fitting window $t \in [t_0, t_f]$ as a sum of damped exponentials. Here, t_0 denotes the starting time of the fit, typically chosen relative to the peak amplitude time t_{peak}. The MPM constructs Hankel matrices from time-shifted samples of the waveform and determines the complex frequencies through a generalized eigenvalue problem. The extraction additionally depends on the pencil size, which specifies the dimensions of the Hankel matrices and therefore influences the stability and accuracy of the frequency extraction. The results of the frequency extraction are shown in Fig.4.3. We see that the extracted frequencies converge to the tabulated QNM frequencies[57]. The right panel also shows that the fundamental mode is significantly more stable than the first and second overtones. This is expected, since the overtones are much more strongly damped than the fundamental mode and therefore decay rapidly. Consequently, they dominate the ringdown signal only over a relatively short time interval, making their frequencies more difficult to extract accurately and more sensitive to the choice of fitting window and other numerical effects.

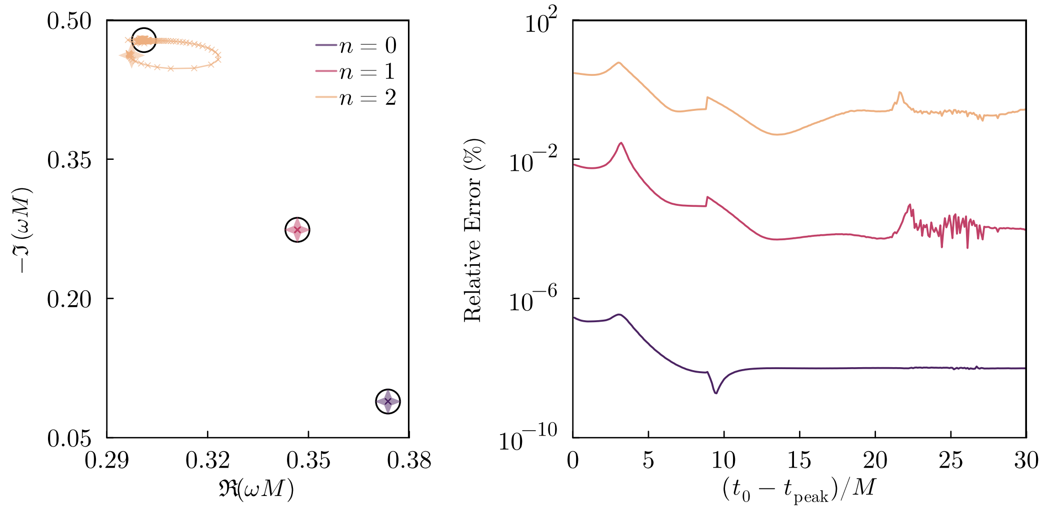

Figure 4.3: Extracted quasinormal-mode frequencies from signals evolved on a Schwarzschild background, in the case of $\ell = 2$ (**left**). The relative error of the extracted QNM frequencies, compared to tabulated QNM in Ref. [57] (**right**). The signals originate from stationary initial data with $\psi_0 = 1$, width $\sigma = 1M$, and center $r_0 = 20M$. The frequencies are obtained using the matrix pencil method with a pencil size $L = N/2$, retaining only the fundamental mode and the first two overtones. The crosses represent the extracted QNM frequencies for $t_0 - t_{\text{peak}} = 30M$.

In addition to the QNM contribution, the signal also contains a late-time power-law tail [55]. Given a set of QNM frequencies $\omega_{\ell n}$, the waveform can therefore be modeled as the sum of k exponentially damped sinusoids together with a late-time tail,

$$M(t) = Q_k(t) + T_r(t), \tag{4.27}$$

$$Q_k(t) = \sum_{n=0}^{k} a_n e^{-i\omega_{\ell n} t + \phi_n}, \tag{4.28}$$

$$T_p(t) = A\,(t - t_0)^{-p}, \tag{4.29}$$

where $\omega_{\ell n}$ denotes the n-th overtone frequency for a given angular number ℓ. In a spherically symmetric background, the QNM spectrum is independent of the azimuthal number m. We can therefore further test the code by fixing the frequencies and the tail exponent r, while fitting the remaining parameters $a_n\,, \phi_n\,, A$, and t_0 using a non-linear least-squares procedure. Since the fitting problem is highly non-linear, accurate initial parameter estimates are essential for robust convergence.

We can quantify the goodness of fit, by considering the mismatch. The mismatch is calculated by comparing the signal to a given model. Given some signal Ψ and discrete time steps T, we can evaluate our model at each of the discrete time steps to get $\Psi_{\text{fit}} = [M(T_0), \ldots, M(T_N)]$. The mismatch is then defined as

$$\mathcal{M} = 1 - \frac{\langle \Psi | \Psi_{\text{fit}} \rangle}{\sqrt{\langle \Psi | \Psi \rangle \langle \Psi_{\text{fit}} | \Psi_{\text{fit}} \rangle}}\,, \tag{4.30}$$

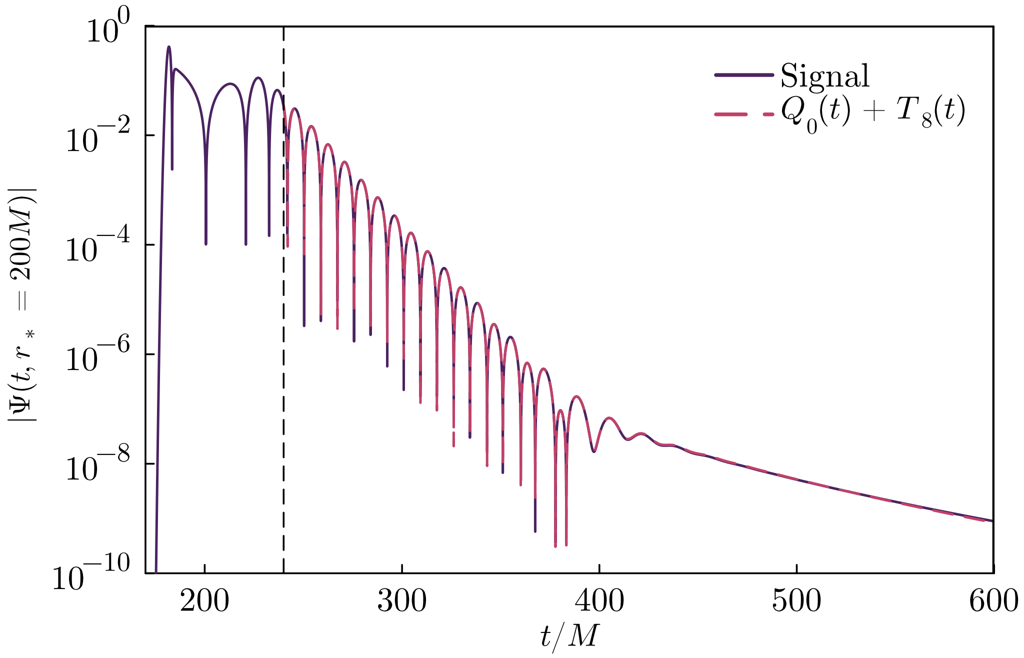

Figure 4.4: Fit to the signal obtained from stationary initial data on a Schwarzschild background in the case of $\ell = 2$, with initial data parameters $\psi_0 = 1$, $\sigma = 1M$, and $r_0 = 20M$. The fitting window begins at $t = 240M$ (black dashed line), chosen to match the initial time used in the matrix pencil method at which the extracted frequency corresponds to the fundamental quasinormal mode and the associated error is minimized (see Fig. 4.3). The fit includes only the fundamental QNM and a power-law tail with exponent $p = 8$, as expected from Ref. [58]. This fit gives a mismatch of $\mathcal{M} \approx 2.3 \times 10^{-3}$

where we the inner product $\langle \cdot | \cdot \rangle$ is calculated as

$$\langle F|G\rangle = \sum_{n=0}^{N} \bar{f}^n g^n \, . \tag{4.31}$$

Figure 4.4 shows the time-domain signal, consisting of an initial prompt response [54] followed by a ringdown phase dominated by exponentially damped black-hole QNMs, and finally a late-time power-law tail. Fitting the signal to the model in Eq. (4.27) yields a mismatch of approximately $\mathcal{M} \approx 2.3 \times 10^{-3}$ when only the fundamental quasinormal mode is included. Although this is larger than the mismatch of $\sim 10^{-8}$ reported in Ref. [59], that analysis included up to seven overtones in the fit. Given that our model includes only the fundamental mode, the obtained mismatch remains reasonable. This level of agreement indicates that the numerical scheme successfully reproduces the expected response of a linearly perturbed Schwarzschild black hole, in accordance with perturbation theory and previous studies [7, 55, 58].

Linear Response of Oscillatons

5

The two benchmark scenarios established high confidence in the numerical scheme outlined in Sec. 4.1, and the method has likewise been verified to maintain fourth-order convergence on the oscillaton background. Having established both the perturbation equations and a reliable evolution framework, we are now in a position to address the central question of this thesis: how do gravitational waves scatter off an oscillaton?

As described in Chap. 2, the oscillaton spacetime is not static, making both the wave equation and the local propagation speed explicitly time dependent. Since this time dependence is periodic with period $T = \pi/\omega$, the perturbation evolves in a dynamically modulated medium for which parametric amplification becomes a natural possibility.

We begin with the simplest initial data, a Gaussian envelope, in order to build intuition for the generic scattering phenomenology of perturbations on an oscillaton background. We then turn to wavepacket initial data with controlled frequency content, allowing us to probe more directly the conditions under which perturbations can extract energy from the background through parametric resonant.

5.1 Gaussian initial data

We begin by analyzing the signal resulting from Gaussian initial data, as described in Sec. 4.2.

This case corresponds to zero average momentum, $\omega_{\mathrm{d}} = 0$, and therefore provides the simplest setting in which to establish the baseline scattering phenomenology of gravitational perturbations on an oscillaton background.

In Fig. 5.1, we show the time-evolution of a wavepacket on the oscillaton spacetime. As one can see, the signal clearly exhibits three distinct stages familiar from the black hole case: a prompt response, followed by a ringdown-like phase, and finally a power-law tail.

In the case of an oscillaton, the effective potential in the wave equation is everywhere strictly decreasing, $\partial_r V(t, r) < 0$, so there are no trapping regions. As a consequence, one expects a full reflection of the wave content, which is consistent with the observed signal.

The prompt responds in the signal is reminiscent of the prompt response we see in the Minkowski and Schwarzschild backgrounds (see Sec. 4.3).

The intermediate stage can be interpreted as a ringdown-like response, even though the oscillaton spacetime is explicitly time dependent and does not strictly admit quasinormal modes. A natural point of comparison is provided by boson stars, which

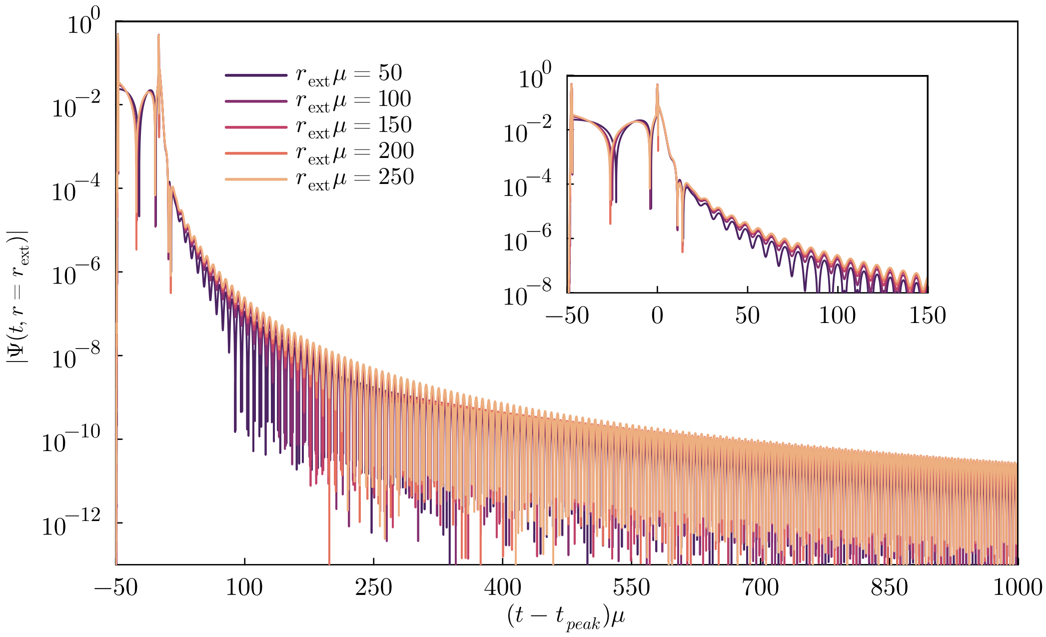

Figure 5.1: The extracted signals at five extraction radii, $r\mu = \{50, 100, 150, 200, 250\}$, for an oscillaton background with Gaussian initial data ($\psi_0 = 1$, $\mu\sigma = 0.2$, $\mu r_0 = 20$, $\ell = 2$) (**main**). Same signals but zoomed in at the ringdown part, showing that the signal only begins to change with respect to extraction radii, when reaching the tail part of the signal (**inset**). The oscillaton configuration corresponds to the maximum-mass solution, as discussed in Chap. 2.

arise as solutions of the Einstein-Klein-Gordon system with a complex scalar field. In contrast to oscillatons, boson star spacetimes are static and spherically symmetric, and therefore admit a well-defined quasinormal mode spectrum. This comparison provides a useful order-of-magnitude check on the ringdown timescale, even though the two configurations are not identical solutions. The relevant frequencies, computed in Ref. [35] for configurations with mass and radius comparable to those of the maximally compact oscillaton, are listed in Table 5.1.

ℓ	n	$\Re(\omega_{\ell n})\mu$	$-\Im(\omega_{\ell n})\mu$
2	0	0.261	0.371
	1	0.455	0.375
4	0	0.695	0.408
	1	0.476	0.456

Table 5.1.: Gravitational quasinormal mode frequencies $\omega_{\ell n}$ for a boson star, with ℓ being denoting the angular mode, and n the overtone number. The boson star configuration has a mass $M \approx 0.633/\mu$, 99th-percentile radius $R \approx 7.068/\mu$, and characteristic frequency $\omega \approx 0.853\,\mu$ [35]. The $\ell = 4$ mode frequencies are calculated by using a Mathematical notebook given directly by Caio Macedo.

Looking at Fig. 5.1, the ringdown signal is most clearly visible for the $\ell = 4$ mode. The waveform exhibits the expected sequence of a prompt response, followed by a damped oscillatory (ringdown-like) phase, and a late-time tail.

To extract quasi-normal mode (QNM) frequencies from the signal using the Matrix Pencil Method (see App. A), a minimal number of oscillations is required in order to reliably resolve the parameters of a damped sinusoid $e^{-\omega_I t}\sin(\omega_R t + \phi)$. In practice, signals shorter than roughly one to two cycles do not provide sufficient phase information for a stable fit.

For $\ell = 4$ (see Fig. 5.2), the ringdown phase is sufficiently well-resolved for this procedure. Applying the Matrix Pencil Method and retaining only the leading contributing modes, we extract two dominant frequencies,

$$\omega_{4,0} \approx 0.918 - 1.094i\,, \tag{5.1}$$

$$\omega_{4,1} \approx -1.883i\,. \tag{5.2}$$

To compare with Ref. [35], one must account for a difference in the normalization of the time coordinate, which introduces a conversion factor of $\sqrt{2}$, i.e. $\omega_{\text{Macedo}} = \omega_{\text{our}}/\sqrt{2}$. After this rescaling, the real part of the fundamental frequency agrees with the boson star value to within 6.6%, while the imaginary part shows a larger deviation. This is not unexpected: the two configurations have similar but not identical masses and radii, the explicit time dependence of the oscillaton may further affect the damping rate, and the ringdown phase contains only a few oscillations, which limits the accuracy of the frequency extraction.

At late times, since the oscillaton spacetime is asymptotically Schwarzschild-like, one expects power-law tails. The signal in Fig. 5.1 appears to consist of two such components: a pure power-law decay and an oscillatory modulated power law. This structure becomes evident when varying the extraction radius, as the relative weight of the two components changes with r. In the absence of a precise theoretical prediction, we model the signal with the ansatz

$$\Psi(t) = \frac{A_{\text{osc}}\cos(kt + \phi_{\text{osc}})}{(t + \delta_{\text{osc}})^{\alpha}} + A_{\text{tail}}(t + \delta_{\text{tail}})^{-\beta}\,, \tag{5.3}$$

where $\Psi(t)$ denotes the time-domain signal. The zero-frequency component decays faster than the oscillatory tail: at large extraction radii the signal is dominated by the pure power law component for a longer stretch of time before the oscillatory tail takes over, consistent with $\alpha > \beta$.

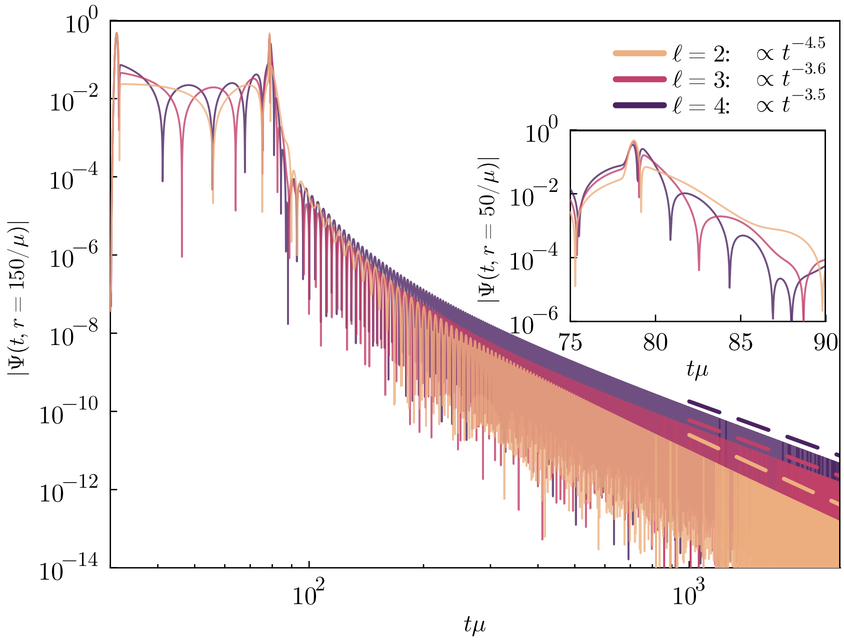

Figure 5.2: Extracted signals at $\mu r = 50$ for Gaussian initial data ($\psi_0 = 1$, $\mu\sigma = 0.2$, $\mu r_0 = 20$) and $\ell = \{2, 3, 4\}$ (solid), together with fits to the late-time oscillatory tail (dashed). The oscillaton configuration corresponds to the maximum-mass solution, as discussed in Chap. 2.

At late times, the signal is expected to be dominated by the oscillatory component of the tail, which takes the form

$$\Psi(t) \sim t^{-\alpha} \cos(\omega t + \phi_{\text{osc}})\,. \tag{5.4}$$

To isolate the envelope of this oscillatory behaviour, we consider the regime $t \gg 0$ and introduce a phase-shifted version of the signal,

$$\Psi_{\text{shift}}(t) = \Psi\left(t - \frac{\pi}{2\omega}\right) \sim t^{-\alpha} \sin(\omega t + \phi_{\text{osc}}) + \mathcal{O}(t^{-\alpha-1})\,. \tag{5.5}$$

Combining the original and shifted signals then allows us to construct the complex quantity

$$S(t) \approx \Psi(t) + i\Psi_{\text{shift}}(t)\,, \tag{5.6}$$

whose magnitude approximately captures the tail envelope. Indeed, taking the absolute value gives

$$\begin{aligned} |S(t)| &\sim t^{-\alpha} |e^{i(\omega t + \phi_{\text{osc}})}| + \mathcal{O}(t^{-\alpha-1}) \\ &= t^{-\alpha} + \mathcal{O}(t^{-\alpha-1})\,. \end{aligned} \tag{5.7}$$

The decay exponent can therefore be extracted through a logarithmic derivative,

$$t\partial_t \ln|S(t)| = -\alpha + \mathcal{O}(t^{-1})\,. \tag{5.8}$$

Applying this procedure to the numerical data, we find that the oscillatory tail exponent remains close to $\alpha \approx 3.5$ for all values of ℓ considered, as shown in Fig. 5.2. Moreover, the extracted exponent appears to converge rapidly toward this value as ℓ increases.

5.2 Wavepacket initial data

While simple Gaussian initial data provides a useful baseline for studying perturbation evolution on an oscillaton spacetime, it does not allow us to clearly distinguish between broadband scattering and a response that is selective to the characteristic oscillaton frequency. In particular, a Gaussian excites a wide range of frequencies simultaneously, making it difficult to determine whether any observed enhancement is associated with the background oscillation frequency of the spacetime.

To gain deeper insight, we therefore consider initial data with a finite central frequency ω_{d}, as described in Sec. 4.2.2, which provides controlled spectral support around a chosen driving frequency. The initial time derivative of the field is chosen such that the wave packet is purely ingoing. In this way, we can precisely control the amount of energy carried by the wave packet sent into the system and directly study how it is transferred during scattering.

5.2.1 The energy of the system

To understand how gravitational perturbations interact with oscillatons, we track the energy carried by gravitational waves propagating away from the system after the scattering process.

The rescaled master function $\chi_{\ell m}$ satisfies Eq.(3.39). We denote by $\bar{\chi}_{\ell m}$ its complex conjugate. Multiplying the equation by $\partial_t\bar{\chi}_{\ell m}$ and adding the complex conjugate of the resulting expression yields a real relation that can be written in the form of a local energy balance law [60]. This procedure is standard for wave equations and effectively isolates a conserved energy density and an associated flux. One obtains

$$\begin{aligned}
0 &= \partial_t\bar{\chi}_{\ell m}\left(-\partial_t^2\chi\ell m + \partial_r\left(\frac{1}{C}\partial_r\chi_{\ell m}\right) - \tilde{V}\chi_{\ell m}\right)\\
&= -\partial_t\left(|\partial_t\chi_{\ell m}|^2 + \frac{1}{C}|\partial_r\chi_{\ell m}|^2 + \tilde{V}|\chi_{\ell m}|^2\right)\\
&\quad + \partial_r\left(\frac{\partial_t\bar{\chi}_{\ell m}\partial_r\chi_{\ell m} + \partial_t\chi_{\ell m}\partial_r\bar{\chi}_{\ell m}}{C}\right) + \frac{\partial_t C}{C^2}|\partial_r\chi_{\ell m}|^2 - \partial_t\tilde{V}|\chi_{\ell m}|^2\,.
\end{aligned} \tag{5.9}$$

The first term defines a local energy density for the perturbation, while the radial derivative term has the form of a total divergence and therefore represents an energy flux. The last two terms arise from the explicit time dependence of the background geometry and describe energy exchange between the oscillaton and the perturbation.

To make this interpretation explicit, we integrate the divergence term over the radial domain. By the fundamental theorem of calculus, a total radial derivative contributes only boundary terms, so that

$$\begin{aligned}\mathcal{F}^{\infty}_{\ell m} &= \int_0^{\infty} \partial_r \left(\frac{\partial_t \bar{\chi}_{\ell m} \partial_r \chi \ell m + \partial_t \chi_{\ell m} \partial_r \bar{\chi}_{\ell m}}{C} \right) \mathrm{d}r \\ &= \left[\frac{\partial_t \bar{\chi}_{\ell m} \partial_r \chi_{\ell m} + \partial_t \chi_{\ell m} \partial_r \bar{\chi}_{\ell m}}{C} \right]_{r=0}^{r=\infty} . \end{aligned} \tag{5.10}$$

Using $\bar{X}Y + X\bar{Y} = 2\mathrm{Re}(\bar{X}Y)$ and imposing regularity at the origin, $\chi_{\ell m}(r=0) = 0$, the contribution from $r = 0$ vanishes. The flux at infinity therefore reduces to

$$\mathcal{F}^{\infty}_{\ell m} = \left. \frac{2\mathrm{Re}(\partial_t \bar{\chi}_{\ell m} \partial_r \chi_{\ell m})}{C} \right|_{r\to\infty} . \tag{5.11}$$

The oscillaton background is asymptotically flat, approaching the Schwarzschild metric as $r \to \infty$, where $C \to 1$ and $\chi_{\ell m} \to \psi^{\mathrm{axial}}_{\ell m}$. Assuming purely outgoing waves at infinity, such that $\partial_t \chi_{\ell m} = -\partial_r \chi_{\ell m}$, the flux simplifies to

$$\mathcal{F}^{\infty}_{\ell m} = 2 |\partial_t \psi^{\mathrm{axial}}_{\ell m}|^2 \Big|_{r\to\infty} . \tag{5.12}$$

To match the conventions in Refs. [50, 61], we include a proper normalization factor. The energy carried to infinity by axial gravitational perturbations is then given by

$$\begin{aligned}\frac{\mathrm{d}E^{\mathrm{axial}}_{\ell m}}{\mathrm{d}t} &= \frac{1}{128\pi} \frac{(\ell+2)!}{(\ell-2)!} \mathcal{F}^{\infty}_{\ell m} \\ &= \frac{1}{64\pi} \frac{(\ell+2)!}{(\ell-2)!} \left| \partial_t \psi^{\mathrm{axial}}_{\ell m} \right|^2 \Bigg|_{r\to\infty} . \end{aligned} \tag{5.13}$$

For the purpose of this study it is not sufficient to only track the total energy flux at infinity; we additionally decompose the flux into ingoing and outgoing components using null coordinates, which allows us to quantify the relative energy carried into and away from the system during scattering

$$\frac{dE^{\mathrm{axial,In}}_{\ell m}}{dt} = \frac{1}{16\pi} \frac{(\ell+2)!}{(\ell-2)!} \left| \partial_v \psi^{\mathrm{axial}}_{\ell m} \right|^2 \Bigg|_{r=r_{\mathrm{ext}}} , \tag{5.14}$$

$$\frac{dE^{\mathrm{axial,Out}}_{\ell m}}{dt} = \frac{1}{16\pi} \frac{(\ell+2)!}{(\ell-2)!} \left| \partial_u \psi^{\mathrm{axial}}_{\ell m} \right|^2 \Bigg|_{r=r_{\mathrm{ext}}} . \tag{5.15}$$

The total energy passing through a large sphere of radius $r_{\rm ext}$ up to a time t is the integral of these fluxes

$$E_{\ell m}^{\rm In/Out}(t) = \int_0^t dt' \frac{dE_{\ell m}^{\rm axial,In/Out}}{dt'} \,. \tag{5.16}$$

Finally, we characterize the energy exchange during the scattering process by calculating the difference between the total outgoing and ingoing energy at the end of the simulation

$$\Delta E_{\ell m}^{\rm end} = E_{\ell m}^{\rm Out}(t_{\rm end}) - E_{\ell m}^{\rm In}(t_{\rm end}) \,. \tag{5.17}$$

It follows that if $\Delta E_{\ell m}^{\rm end} < 0$, the perturbation has lost energy during the scattering process, effectively transferring energy to the oscillaton; conversely, if $\Delta E_{\ell m}^{\rm end} > 0$, the perturbation has gained energy from the background.

5.3 Oscillatons as parametric drivers

To understand the resonance structure of the oscillaton spacetime, we treat the wave equation as a Hill-type equation with operator coefficients. By expanding the time-dependent coefficients of Eq. (3.39) into a Fourier series, we obtain

$$-\partial_t^2\chi + \mathcal{L}_r^{(0)}\chi + \sum_{k=1}^{\infty} \cos^k(2\omega t)\mathcal{L}_r^{(k)}\chi = 0 \,, \tag{5.18}$$

where $\mathcal{L}_r^{(0)}$ is the static part of the radial operator and the $\mathcal{L}_r^{(k)}$ terms represent the higher harmonics of the background oscillation. We project the solution onto an eigenbasis $\{u_n(r)\}$ of the zeroth-order operator, defined by $\mathcal{L}_r^{(0)}u_n(r) = -\Omega_n^2 u_n(r)$, where Ω_n are the natural frequencies of each mode. Writing the full solution as $\chi(t,r) = \sum_n q_n(t)u_n(r)$ and projecting onto each eigenmode, we find a system of coupled equations

$$\partial_t^2 q_n + \Omega_n^2 q_n + \sum_{k=1,m} \cos^k(2\omega t)M_{mn}^{(k)}q_m = 0 \,, \tag{5.19}$$

where the mixing matrices are defined by the overlap integrals

$$M_{mn}^{(k)} \equiv -\int_0^{\infty} dr(\bar{u}_m\mathcal{L}_r^{(k)}u_n) \,. \tag{5.20}$$

By assuming the dynamics are dominated by the diagonal terms, the system reduces to a set of independent parametric oscillators.

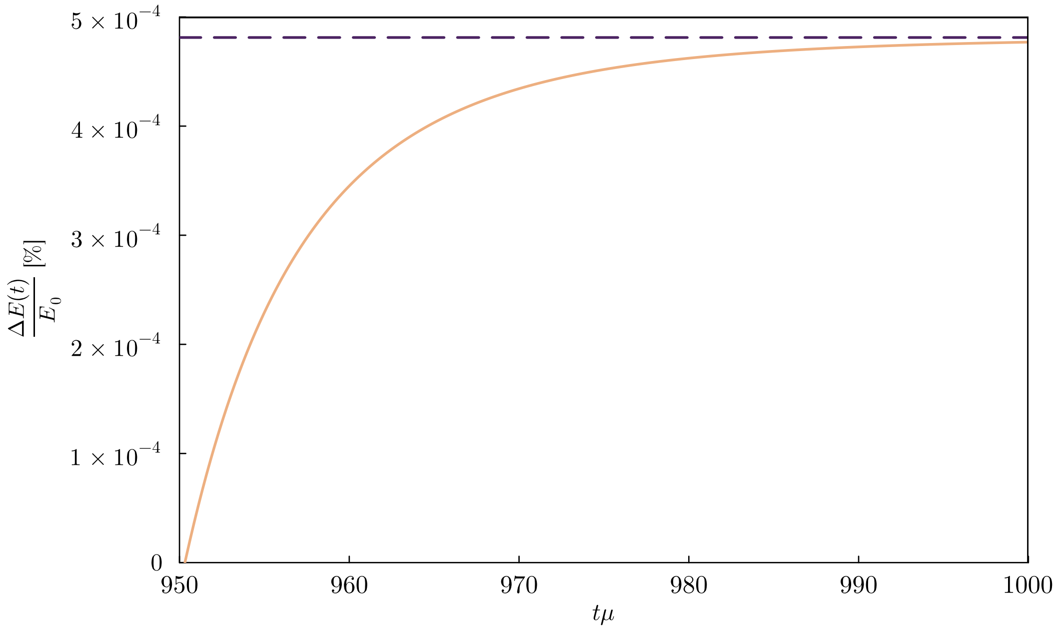

Figure 5.3: An example of the energy change as calculated by Eq. 5.17 and normalized by the total ongoing energy. The final energy change is shown as a dashed line. The initial data is a Gaussian profile with $\psi_0 = 0$, $\sigma\mu = 20$, $r_0\mu = 500$ and $\omega_\mathrm{d} = 0$, evolved on a maximum mass oscillaton configuration.

As a first illustration of the energy exchange between the perturbation and the oscillaton, Fig. 5.3 shows the result of sending in a Gaussian with zero driving frequency, $\omega_\mathrm{d} = 0$. Despite this, the outgoing energy exceeds the ingoing energy, suggesting that the perturbation has gained energy from the background. At first glance this appears to contradict the Mathieu equation analysis, which predicts no resonance at zero frequency. The resolution lies in the frequency content of the initial data: a spatially narrow Gaussian is broad in frequency space, with a spectral width of order $1/\sigma^2$. The initial data therefore contains contributions spanning a wide range of frequencies, some of which inevitably overlap with the resonance bands of the system. The observed energy gain is thus a natural consequence of this broadband excitation rather than a violation of the resonance condition.

5.3.1 Small mass configurations

We first consider low-compactness oscillatons, where the periodic modulation of the spacetime is weak, in order to test whether the perturbation dynamics reduce to the single-band resonance structure predicted by the Mathieu equation. In this limit, the oscillaton oscillates with small amplitude, and the time-dependent components of the metric are heavily suppressed relative to the static background. We may therefore approximate $|c_1| \ll |c_0|$ and $|b_1| \ll |b_0|$, such that the background is well described by a nearly static spacetime with a small periodic modulation. This is precisely the regime in which the Mathieu equation provides an accurate description of the perturbation dynamics, and we therefore expect a single dominant primary resonance band.

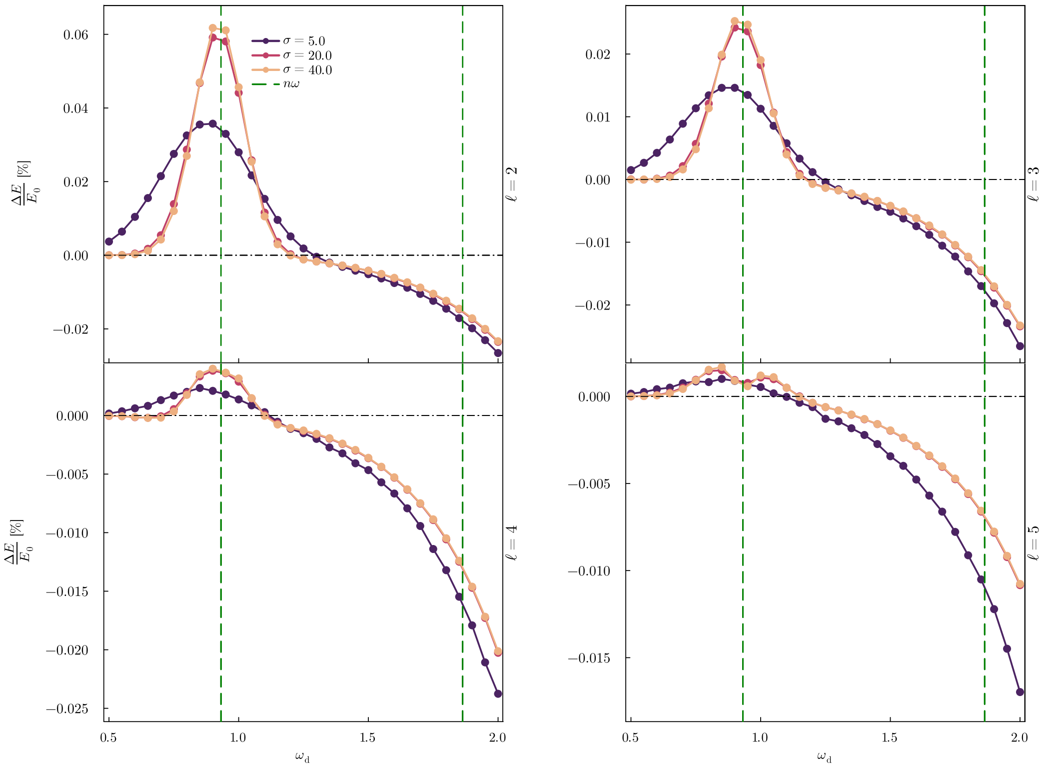

Figure 5.4: Energy change as a function of the driving frequency ω_d for a low-compactness configuration ($\phi_1(0) = 0.15$, $\omega \approx 0.932\mu$), for four different angular modes $\ell = \{2, 3, 4, 5\}$. The peak near $\omega_\mathrm{d} \approx \omega$ confirms the primary resonance predicted by the Mathieu equation. The green dotted lines represent $\omega_\mathrm{d} = \{\omega, 2\omega\}$

The expansion (5.18) is dominated by the first harmonic ($k = 1$), in which the radial operators simplify to

$$\mathcal{L}_r^{(0)} = \partial_r\left(\frac{1}{c_0}\partial_r\right) - \tilde{V}_0\,, \tag{5.21}$$

$$\mathcal{L}_r^{(1)} = \partial_r\left(\frac{c_1}{c_0}\partial_r\right) + \tilde{V}_1\,, \tag{5.22}$$

where $\tilde{V}_0$ and $\tilde{V}_1$ are the leading terms of the potential expansion. Retaining only the diagonal terms of $M^{(1)}_{mn}$, the evolution of each mode reduces to a simple Mathieu equation

$$\partial_t^2 q_n + [\Omega_n^2 + M^{(1)}_{nn}\cos(2\omega t)]q_n = 0\,, \tag{5.23}$$

which predicts a primary resonance band centered at $\Omega_n \approx \omega$. The off-diagonal terms $M^{(1)}_{mn}$ with $m \neq n$ couple different modes together, and their neglect is the key approximation of this analysis. For a low-compactness oscillaton, the coupling between modes is weak and this diagonal approximation is well justified; for more compact configurations, mode mixing may become important.

The predicted resonance is confirmed in Fig. 5.4, where the energy change ΔE is plotted as a function of the driving frequency ω_{d}. The energy gain is sharply peaked near $\omega_{\mathrm{d}} \approx \omega$, consistent with the primary resonance band of the Mathieu equation.

We also observe that the energy extraction becomes saturated beyond a certain width of the initial wavepacket. In particular, the resonance peaks for initial data with $\sigma\mu = 20$ and $\sigma\mu = 40$ behave almost identically. This is physically reasonable, since once the wavepacket width becomes comparable to the size of the oscillaton, the system effectively probes the entire background rather than a localized region. In this regime, further increasing the width does not lead to additional energy transfer, and the response becomes insensitive to further broadening of the initial data.

Fig. 5.4 also reveals a systematic feature beyond the resonance region: as the driving frequency is increased past the dominant resonance peak, the energy change ΔE becomes persistently negative, indicating that the perturbation loses energy to the background. While this could reflect a physical response to off-resonant driving, it may equally well originate from numerical effects. We observe that this behaviour appears with similar magnitude and scaling across all four ℓ modes. Since the spatial resolution is kept fixed across all simulations while only the initial conditions are varied, the observed energy loss may be associated with finite-resolution effects, which become more pronounced when the perturbation overlaps more strongly with the potential near the origin. The onset of this behaviour occurs only beyond the first few resonance peaks, with the precise location depending on the oscillaton background.

5.3.2 Maximum mass oscillaton

We next turn to the maximum-mass configuration, where the oscillaton dynamics become strongly time dependent and higher harmonics of the background can no longer be neglected. In this regime, the perturbation dynamics are no longer dominated by a single harmonic, and the simple Mathieu-equation description of the previous section is therefore expected to break down. A more accurate description now requires retaining additional terms in the Fourier expansion of the Hill-type equation. The radial derivative operators therefore take the more general form

$$\mathcal{L}_r^{(k)} = (-1)^{k+1}\partial_r\left(\frac{c_1(r)^k}{c_0(r)^{k+1}}\partial_r\right) + \tilde{V}_k\,. \tag{5.24}$$

Retaining terms up to the second harmonic and expanding the powers of the cosine, the evolution equation for each diagonal mode becomes

$$\partial_t^2 q_n + \left[\frac{1}{2}(M_{nn}^{(2)} + 2\Omega_n^2) + M_{nn}^{(1)}\cos(2\omega t) + \frac{1}{2}M_{nn}^{(2)}\cos(4\omega t)\right] q_n = 0\,. \tag{5.25}$$

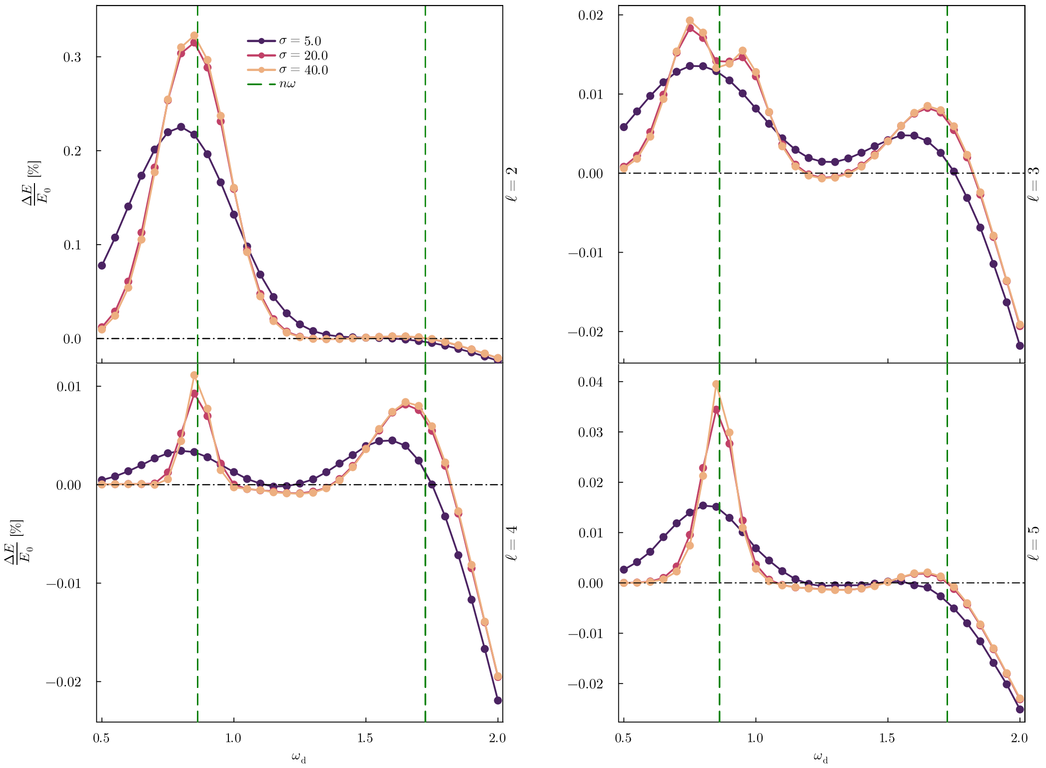

Figure 5.5: Energy change for the maximum mass configuration ($\phi_1(r=0) \approx 0.334\,,\ \omega \approx 0.862\mu$). Two distinct peaks near integer multiples of the oscillaton frequency demonstrate the role of higher-order harmonics in the background driving. The figure shows four plots, one for each value of $\ell = \{2, 3, 4, 5\}$. The dotted green lines represent $\omega_{\mathrm{d}} = \{\omega, 2\omega\}$.

Compared to the Mathieu equation of the previous section, two new effects appear. The $M^{(2)}_{nn}$ term shifts the effective frequency of the primary resonance, while the $\cos(4\omega t)$ term opens a secondary resonance band near $\omega_d \approx 2\omega$. Both effects are visible in Fig. 5.5: the energy extraction now peaks at two distinct driving frequencies, corresponding to the first two integer multiples of the oscillaton frequency, in contrast to the single peak seen in the low-compactness case. We also see that the second peak has shifted, just like Eq. (5.25) predicts.

As in the low-mass limit, we again observe that the energy exchange saturates once the width of the initial wavepacket is increased beyond a certain point. Beyond this threshold, further broadening does not lead to additional energy transfer, indicating that the system has effectively reached a regime where it probes the full spatial extent of the oscillaton.

While the low-mass configurations exhibited narrow, Mathieu-like resonance peaks, the maximum-mass oscillaton shows a broader frequency window where $\Delta E > 0$. This indicates that in the strongly self-gravitating regime, the energy transfer becomes less sensitive to precise frequency matching between ω_{d} and ω. This behaviour is consistent with the analysis in Sec.3.2, where Fig.3.1 shows that the resonance bands broaden as the effective coupling strength q increases. In the present system, increasing the oscillaton mass enhances the amplitude of the time-dependent metric component, which in turn increases the coefficient $M^{(1)}_{nn}$. This provides a natural explanation for the observed widening of the resonance structure.

5.3.3 Energy gain at resonance

Having established the resonance structure for individual oscillaton configurations, we now ask how the energy exchange depends on the oscillaton configuration itself. Since the maximum energy transfer occurs at the primary resonance $\omega_\mathrm{d} \approx \omega$, we fix the driving frequency accordingly and vary the central scalar field value $\phi_1(r = 0)$, sweeping across the full range of oscillaton configurations from low to high compactness.

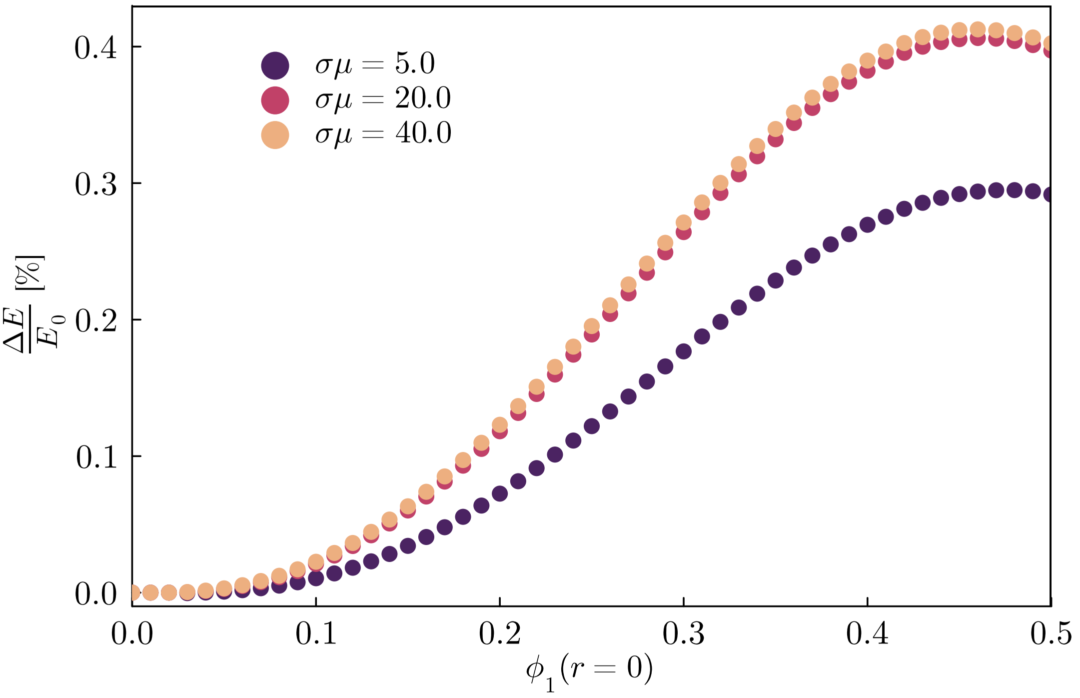

Figure 5.6: The energy is shown as a function of the oscillaton configuration, parameterized by the central scalar field value, as described in Chapter 2, for the $\ell = 2$ case. We study how the energy change depends on the oscillaton configuration for three different initial wavepacket widths, $\sigma\mu = 5, 20, 40$. The driving frequency is chosen as $\omega_\mathrm{d} = \omega[\phi_1(r = 0)]$, corresponding to the oscillaton configuration in each simulation. Consequently, when the oscillaton configuration is varied, the driving frequency changes accordingly.

Figure 5.6 shows that the energy gain generally increases with the central scalar field value, reaching a maximum at approximately $\phi_1(r = 0) \approx 0.45$. Interestingly, this peak occurs at a higher central density than that of the maximum mass configuration. This is consistent with the Mathieu equation picture developed in the previous subsections: the resonance strength is controlled by the coupling coefficients $M^{(1)}_{nn}$, which are set by the amplitude of the oscillatory components of the metric rather than its static part. As the configuration becomes more compact, these oscillatory components grow, enhancing the parametric driving even as the total mass begins to decrease along the high-density branch. The energy gain therefore tracks the oscillatory amplitude of the background rather than its mass, which is a direct consequence of the parametric nature of the interaction.

5.4 Summary of results and discussion

These results demonstrate that oscillatons act as parametric drivers, where the energy exchange between the background and the perturbation is governed by the compactness of the configuration and the angular mode ℓ. For low-compactness configurations, the energy gain is sharply peaked at a single driving frequency $\omega_{\rm d} \approx \omega$, consistent with the primary resonance band expected from a simple Mathieu equation analysis. As we move toward maximum mass configurations, this simple structure breaks down and two distinct resonance peaks emerge, corresponding to the first two integer multiples of the oscillaton frequency. This dual-peak structure becomes increasingly pronounced for higher multipole modes; for $\ell = 3$ and $\ell = 4$, the second peak becomes comparable in magnitude to the first. Even a wavepacket with zero driving frequency is found to gain energy from the background, a consequence of its broad spectral content in frequency space overlapping with the resonance bands of the system.

The strength of the resonance is primarily controlled by the amplitude of the oscillatory components of the metric, rather than the total mass of the oscillaton. The energy gain increases with the central scalar field value $\phi_1(r = 0)$, reaching a maximum beyond the maximum mass configuration on the high-compactness branch, where the metric oscillations are most pronounced.

The heightened sensitivity of higher ℓ modes to the background dynamics is also manifest in the time-domain signals from Gaussian initial data. For larger ℓ, the oscillatory part of the late-time tail carries a significantly larger relative amplitude, suggesting that large ℓ modes are more sensitive to the oscillatory part of the oscillaton.

While the initial ringdown phase is largely determined by the average potential, the late-time behavior and the energy extraction efficiency are dominated by the explicit time-dependence of the spacetime.

We note several limitations of the present analysis. The mode-coupling structure was analyzed by only taking the diagonal components of the mode-coupling matrix, neglecting off-diagonal mixing between different radial eigenmodes. This was used as a qualitative framework to interpret the observed resonance peaks rather than to derive quantitative predictions. For low-compactness configurations this approximation is well justified, but for more compact backgrounds mode mixing may become significant and could modify the resonance structure quantitatively.

Conclusions and Outlook

6

In this thesis, we have investigated how axial gravitational perturbations interact with oscillatons in the time domain, with particular focus on the role played by the explicit time-dependence of the oscillaton background. By numerically evolving the axial perturbation equation on the oscillaton backgrounds, we have shown that the periodic nature of the spacetime acts as a parametric driver, enabling resonant energy exchange between gravitational perturbations and these oscillatons. Resonant amplification occurs when the frequency of the perturbation is tuned to integer multiples of the fundamental oscillaton frequency, and the structure of these resonance peaks can be understood through the Mathieu-like analysis, which provides a natural explanation for understanding both their location and multiplicity. We have further shown that this effect strengthens as the central scalar-field amplitude is increased, reflecting the growing influence of the time-dependent background as the oscillaton becomes more massive and compact.

These findings have potential observational significance. A single gravitational-wave signal interacting with an oscillaton-like structure would likely be difficult to distinguish from other astrophysical effects. However, if oscillaton-like structures were to form in abundance, their cumulative effect on the stochastic gravitational-wave background could, in principle, produce a detectable and frequency-dependent imprint. Crucially, the location of the resonance peaks is set by the characteristic oscillaton frequency, which is itself controlled by the scalar-field mass. Any such spectral feature would therefore carry direct information about the underlying field parameters. A quantitative assessment of detectability, and of potential degeneracies with other astrophysical effects, lies beyond the scope of this work, but represents a natural and compelling direction for future investigation.

Looking ahead, there are a number of directions worth exploring. The present analysis is restricted to axial gravitational perturbations, which decouple from the scalar-field sector at linear order. Including the polar sector would introduce direct coupling between metric and scalar degrees of freedom, and is expected to yield a richer resonance structure. On the observational side, a full treatment of the stochastic gravitational-wave background propagating through a distribution of oscillatons would be the most direct path toward assessing whether such effects are detectable. It would also be interesting to model gravitational-wave generation through a localised source, such as a compact object moving through the oscillaton background, which would connect the resonance physics identified here to concrete waveform generation and more direct observational scenarios. Finally, if oscillaton-like structures were to form on sufficiently large scales, they could in principle also act as gravitational lenses for passing gravitational waves, offering yet another observational handle on the properties of ultralight scalar-field dark matter.Finally, oscillatons have been proposed as models for dark matter halos, which raises the question of how gravitational waves are lensed by such structures. Since lensing is sensitive to the mass distribution of the lens, and the oscillaton's characteristic scale is set by the scalar-field mass, this could offer yet another observational handle on the properties of ultralight scalar-field dark matter.

Bibliography

7

[1] Werner Israel. „Event horizons in static vacuum space-times“. In: *Phys. Rev.* 164 (1967), pp. 1776–1779.

[2] Werner Israel. „Event horizons in static electrovac space-times“. In: *Commun. Math. Phys.* 8 (1968), pp. 245–260.

[3] B. Carter. „Axisymmetric Black Hole Has Only Two Degrees of Freedom“. In: *Phys. Rev. Lett.* 26 (1971), pp. 331–333.

[4] S. W. Hawking. „Black holes in general relativity“. In: *Commun. Math. Phys.* 25 (1972), pp. 152–166.

[5] D. C. Robinson. „Uniqueness of the Kerr black hole“. In: *Phys. Rev. Lett.* 34 (1975), pp. 905–906.

[6] P. O. Mazur. „PROOF OF UNIQUENESS OF THE KERR-NEWMAN BLACK HOLE SOLUTION“. In: *J. Phys. A* 15 (1982), pp. 3173–3180.

[7] Emanuele Berti, Vitor Cardoso, and Andrei O. Starinets. „Quasinormal modes of black holes and black branes“. In: *Class. Quant. Grav.* 26 (2009), p. 163001. arXiv: `0905.2975 [gr-qc]`.

[8] Emanuele Berti *et al.* „Black hole spectroscopy: from theory to experiment“. In: (May 2025). arXiv: `2505.23895 [gr-qc]`.

[9] B. P. Abbott *et al.* „Observation of Gravitational Waves from a Binary Black Hole Merger“. In: *Phys. Rev. Lett.* 116.6 (2016), p. 061102. arXiv: `1602.03837 [gr-qc]`.

[10] B. P. Abbott *et al.* „GWTC-1: A Gravitational-Wave Transient Catalog of Compact Binary Mergers Observed by LIGO and Virgo during the First and Second Observing Runs“. In: *Phys. Rev. X* 9.3 (2019), p. 031040. arXiv: `1811.12907 [astro-ph.HE]`.

[11] R. Abbott *et al.* „GWTC-2: Compact Binary Coalescences Observed by LIGO and Virgo During the First Half of the Third Observing Run“. In: *Phys. Rev. X* 11 (2021), p. 021053. arXiv: `2010.14527 [gr-qc]`.

[12] R. Abbott *et al.* „GWTC-3: Compact Binary Coalescences Observed by LIGO and Virgo during the Second Part of the Third Observing Run“. In: *Phys. Rev. X* 13.4 (2023), p. 041039. arXiv: `2111.03606 [gr-qc]`.

[13] N. Aghanim *et al.* „Planck 2018 results. VI. Cosmological parameters“. In: *Astron. Astrophys.* 641 (2020). [Erratum: Astron.Astrophys. 652, C4 (2021)], A6. arXiv: `1807.06209 [astro-ph.CO]`.

[14] Vera C. Rubin and W. Kent Ford Jr. „Rotation of the Andromeda Nebula from a Spectroscopic Survey of Emission Regions“. In: *Astrophys. J.* 159 (1970), pp. 379–403.

[15] K. C. Freeman. „On the disks of spiral and SO Galaxies“. In: *Astrophys. J.* 160 (1970), p. 811.

[16] J. P. Ostriker and P. J. E. Peebles. „A Numerical Study of the Stability of Flattened Galaxies: or, can Cold Galaxies Survive?“ In: *Astrophys. J.* 186 (1973), pp. 467–480.

[17] M. S. Roberts and R. N. Whitehurst. „The rotation curve and geometry of M31 at large galactocentric distances.“ In: 201 (Oct. 1975), pp. 327–346.

[18] V. C. Rubin, N. Thonnard, and W. K. Ford Jr. „Rotational properties of 21 SC galaxies with a large range of luminosities and radii, from NGC 4605 /R = 4kpc/ to UGC 2885 /R = 122 kpc/“. In: *Astrophys. J.* 238 (1980), p. 471.

[19] Massimo Persic, Paolo Salucci, and Fulvio Stel. „The Universal rotation curve of spiral galaxies: 1. The Dark matter connection“. In: *Mon. Not. Roy. Astron. Soc.* 281 (1996), p. 27. arXiv: `astro-ph/9506004`.

[20] Fabio Iocco, Miguel Pato, and Gianfranco Bertone. „Evidence for dark matter in the inner Milky Way“. In: *Nature Phys.* 11 (2015), pp. 245–248. arXiv: `1502.03821 [astro-ph.GA]`.

[21] Henk Hoekstra, Howard K. C. Yee, and Michael D. Gladders. „Properties of galaxy dark matter halos from weak lensing“. In: *IAU Symp.* 220 (2004). Ed. by S. D. Ryder, D. J. Pisano, M. A. Walker, and K. C. Freeman, p. 439. arXiv: `astro-ph/0310756`.

[22] Douglas Clowe, Marusa Bradac, Anthony H. Gonzalez, Maxim Markevitch, Scott W. Randall, Christine Jones, and Dennis Zaritsky. „A direct empirical proof of the existence of dark matter“. In: *Astrophys. J. Lett.* 648 (2006), pp. L109–L113. arXiv: `astro-ph/0608407`.

[23] Volker Springel *et al.* „Simulating the joint evolution of quasars, galaxies and their large-scale distribution“. In: *Nature* 435 (2005), pp. 629–636. arXiv: `astro-ph/0504097`.

[24] Wayne Hu, Rennan Barkana, and Andrei Gruzinov. „Cold and fuzzy dark matter“. In: *Phys. Rev. Lett.* 85 (2000), pp. 1158–1161. arXiv: `astro-ph/0003365`.

[25] Lam Hui, Jeremiah P. Ostriker, Scott Tremaine, and Edward Witten. „Ultralight scalars as cosmological dark matter“. In: *Phys. Rev.* D95.4 (2017), p. 043541. arXiv: `1610.08297 [astro-ph.CO]`.

[26] Lam Hui. „Wave Dark Matter“. In: *Ann. Rev. Astron. Astrophys.* 59 (2021), pp. 247–289. arXiv: `2101.11735 [astro-ph.CO]`.

[27] Keir K. Rogers and Hiranya V. Peiris. „Strong Bound on Canonical Ultralight Axion Dark Matter from the Lyman-Alpha Forest“. In: *Phys. Rev. Lett.* 126.7 (2021), p. 071302. arXiv: `2007.12705 [astro-ph.CO]`.

[28] Vid Iršič, Matteo Viel, Martin G. Haehnelt, James S. Bolton, and George D. Becker. „First constraints on fuzzy dark matter from Lyman-α forest data and hydrodynamical simulations“. In: *Phys. Rev. Lett.* 119.3 (2017), p. 031302. arXiv: `1703.04683 [astro-ph.CO]`.

[29] Steven L. Liebling and Carlos Palenzuela. „Dynamical boson stars“. In: *Living Rev. Rel.* 26.1 (2023), p. 1. arXiv: `1202.5809 [gr-qc]`.

[30] David J. Kaup. „Klein-Gordon Geon“. In: *Phys. Rev.* 172 (1968), pp. 1331–1342.

[31] Remo Ruffini and Silvano Bonazzola. „Systems of selfgravitating particles in general relativity and the concept of an equation of state“. In: *Phys. Rev.* 187 (1969), pp. 1767–1783.

[32] J. D. Breit, S. Gupta, and A. Zaks. „COLD BOSE STARS“. In: *Phys. Lett. B* 140 (1984), pp. 329–332.

[33] M. Colpi, S. L. Shapiro, and I. Wasserman. „Boson Stars: Gravitational Equilibria of Selfinteracting Scalar Fields“. In: *Phys. Rev. Lett.* 57 (1986), pp. 2485–2488.

[34] Franz E. Schunck and Eckehard W. Mielke. „General relativistic boson stars“. In: *Class. Quant. Grav.* 20 (2003), R301–R356. arXiv: `0801.0307 [astro-ph]`.

[35] Caio F. B. Macedo, Paolo Pani, Vitor Cardoso, and Luís C. B. Crispino. „Astrophysical signatures of boson stars: quasinormal modes and inspiral resonances“. In: *Phys. Rev. D* 88.6 (2013), p. 064046. arXiv: `1307.4812 [gr-qc]`.

[36] E. Seidel and W. M. Suen. „Oscillating soliton stars“. In: *Phys. Rev. Lett.* 66 (1991), pp. 1659–1662.

[37] Don N. Page. „Classical and quantum decay of oscillatons: Oscillating selfgravitating real scalar field solitons“. In: *Phys. Rev. D* 70 (2004), p. 023002. arXiv: `gr-qc/0310006`.

[38] Miguel Alcubierre, Ricardo Becerril, Siddhartha F. Guzman, Tonatiuh Matos, Dario Nunez, and L. Arturo Urena-Lopez. „Numerical studies of Phi**2 oscillatons“. In: *Class. Quant. Grav.* 20 (2003), pp. 2883–2904. arXiv: `gr-qc/0301105`.

[39] Pau Amaro-Seoane *et al.* „Laser Interferometer Space Antenna“. In: (Feb. 2017). arXiv: `1702.00786 [astro-ph.IM]`.

[40] M. Punturo *et al.* „The Einstein Telescope: A third-generation gravitational wave observatory“. In: *Class. Quant. Grav.* 27 (2010). Ed. by Fulvio Ricci, p. 194002.

[41] Mateja Bošković, Francisco Duque, Miguel C. Ferreira, Filipe S. Miguel, and Vitor Cardoso. „Motion in time-periodic backgrounds with applications to ultralight dark matter haloes at galactic centers“. In: *Phys. Rev. D* 98 (2018), p. 024037. arXiv: `1806.07331 [gr-qc]`.

[42] L. Arturo Urena-Lopez. „Oscillatons revisited“. In: *Class. Quant. Grav.* 19 (2002), pp. 2617–2632. arXiv: `gr-qc/0104093`.

[43] L. A. Urena-Lopez, T. Matos, and R. Becerril. „Inside oscillatons“. In: *Class. Quant. Grav.* 19 (2002), pp. 6259–6277.

[44] Gyula Fodor, Peter Forgacs, and Mark Mezei. „Mass loss and longevity of gravitationally bound oscillating scalar lumps (oscillatons) in D-dimensions“. In: *Phys. Rev. D* 81 (2010), p. 064029. arXiv: `0912.5351 [gr-qc]`.

[45] Philippe Grandclement, Gyula Fodor, and Peter Forgacs. „Numerical simulation of oscillatons: extracting the radiating tail“. In: *Phys. Rev. D* 84 (2011), p. 065037. arXiv: `1107.2791 [gr-qc]`.

[46] Don N. Page. „Classical and quantum decay of oscillations: Oscillating self-gravitating real scalar field solitons“. In: *Phys. Rev. D* 70 (2 July 2004), p. 023002.

[47] Valeria Ferrari, Leonardo Gualtieri, and Paolo Pani. *General Relativity and its Applications: Black Holes, Compact Stars and Gravitational Waves*. 1st ed. CRC Press, 2020. Chap. 15.2.

[48] Tullio Regge and John A. Wheeler. „Stability of a Schwarzschild singularity“. In: *Phys. Rev.* 108 (1957), pp. 1063–1069.

[49] Michele Maggiore. „Black-hole perturbation theory“. In: *Gravitational Waves: Volume 2: Astrophysics and Cosmology*. Oxford University Press, Mar. 2018. eprint: `https://academic.oup.com/book/0/chapter/369006987/chapter-pdf/45395523/oso-9780198570899-chapter-3.pdf`.

[50] Karl Martel and Eric Poisson. „Gravitational perturbations of the Schwarzschild spacetime: A Practical covariant and gauge-invariant formalism“. In: *Phys. Rev. D* 71 (2005), p. 104003. arXiv: `gr-qc/0502028`.

[51] Émile Mathieu. „Mémoire sur le mouvement vibratoire d’une membrane de forme elliptique.“ fre. In: *Journal de Mathématiques Pures et Appliquées* 13 (1868), pp. 137–203.

[52] Carl M. Bender and Steven A. Orszag. *Advanced Mathematical Methods for Scientists and Engineers I*. Springer, 1999.

[53] Bernard Deconinck and J. Nathan Kutz. „Computing spectra of linear operators using the Floquet–Fourier–Hill method“. In: *Journal of Computational Physics* 219.1 (2006), pp. 296–321.

[54] Edward W. Leaver. „Spectral decomposition of the perturbation response of the Schwarzschild geometry“. In: *Phys. Rev. D* 34 (1986), pp. 384–408.

[55] Richard H. Price. „Nonspherical perturbations of relativistic gravitational collapse. 1. Scalar and gravitational perturbations“. In: *Phys. Rev. D* 5 (1972), pp. 2419–2438.

[56] Y. Hua and T.K. Sarkar. „Generalized pencil-of-function method for extracting poles of an EM system from its transient response“. In: *IEEE Transactions on Antennas and Propagation* 37.2 (1989), pp. 229–234.

[57] Rico K. L. Lo, Leart Sabani, and Vitor Cardoso. „Quasinormal modes and excitation factors of Kerr black holes“. In: *Phys. Rev. D* 111.12 (2025), p. 124002. arXiv: `2504.00084 [gr-qc]`.

[58] Richard H. Price and Lior M. Burko. „Late time tails from momentarily stationary, compact initial data in Schwarzschild spacetimes“. In: *Phys. Rev. D* 70 (2004), p. 084039. arXiv: `gr-qc/0408077`.

[59] Vishal Baibhav, Mark Ho-Yeuk Cheung, Emanuele Berti, Vitor Cardoso, Gregorio Carullo, Roberto Cotesta, Walter Del Pozzo, and Francisco Duque. „Agnostic black hole spectroscopy: Quasinormal mode content of numerical relativity waveforms and limits of validity of linear perturbation theory“. In: *Phys. Rev. D* 108.10 (2023), p. 104020. arXiv: `2302.03050 [gr-qc]`.

[60] E. C. Zachmanoglou and Dale W. Thoe. *Introduction to partial differential equations with applications*. eng. New York: Dover Publications, Inc., 1986.

[61] K. S. Thorne. „Multipole Expansions of Gravitational Radiation“. In: *Rev. Mod. Phys.* 52 (1980), pp. 299–339.

[62] Gene H. Golub and Charles F. Van Loan. *Matrix computations.* eng. 4. ed. Johns Hopkins studies in the mathematical sciences. 2013 - 2013.

A

Matrix Pencil Method

The Matrix Pencil method, as described in Ref. [56], begins by assuming that the data can be modeled as a superposition of M damped harmonic modes, namely

$$y_n = \sum_{i=1}^{M} c_i z_i^n \,, \qquad \text{with} \qquad z_i = e^{s_i \Delta t} \,. \tag{A.1}$$

Here, the complex parameters s_i encode the oscillation frequencies and damping rates of the individual modes. The purpose of the matrix pencil algorithm is then to estimate the corresponding exponential parameters z_i, or equivalently the poles s_i, directly from the sampled data. Given a dataset $F = [f_0, f_1, \dots, f_N]$, we first construct the Hankel matrix

$$Y_0 = \begin{bmatrix} f_0 & f_1 & \cdots & f_L \\ f_1 & f_2 & & \\ \vdots & & \ddots & \vdots \\ f_{N-L-1} & & \cdots & f_{N-1} \end{bmatrix} . \tag{A.2}$$

We then define the time-shifted Hankel matrix

$$Y_1 = \begin{bmatrix} f_1 & f_2 & \cdots & f_{L+1} \\ f_2 & f_3 & & \\ \vdots & & \ddots & \vdots \\ f_{N-L} & & \cdots & f_N \end{bmatrix} . \tag{A.3}$$

Both are $L \times (N-L-1)$ matrices. The exponential parameters z_i are then obtained by solving the generalized eigenvalue problem

$$Y_1 v_i - z_i Y_0 v_i = 0. \tag{A.4}$$

To understand why this procedure recovers the poles of the signal, let us consider the special choice $L = \frac{N-1}{2}$, for which the Hankel matrices become square. In this case, Y_0 admits the factorization

$$Y_0 = V C V^T \,, \tag{A.5}$$

where C is a diagonal matrix containing the coefficients c_i, and V is the Vandermonde matrix

$$V = \begin{bmatrix} 1 & 1 & \cdots & 1 \\ z_1 & z_2 & & z_M \\ \vdots & & \ddots & \vdots \\ z_1^{\frac{N-1}{2}} & & \cdots & z_M^{\frac{N-1}{2}} \end{bmatrix} . \tag{A.6}$$

Similarly, the shifted Hankel matrix can be written as

$$Y_2 = VCZV^T, \qquad\qquad Z = diag(z_1, z_2, \ldots, z_M). \tag{A.7}$$

The eigenvalue problem may then be rewritten as

$$\begin{aligned} 0 = \det(Y_1 - \lambda Y_0) &= \det\left(VCZV^T - \lambda VCV^T\right) \\ &= \det\left(VC(Z - \lambda I)V^T\right) \\ &= \det(VC)\det(Z - \lambda I)\det\left(V^T\right) . \end{aligned} \tag{A.8}$$

Provided that $\det(VC) \neq 0$ and $\det(V^T) \neq 0$, this reduces to

$$det(Z - \lambda I) = 0\,, \tag{A.9}$$

which implies that the eigenvalues satisfy $\lambda = z_i$. The poles of the signal are therefore recovered directly from the generalized eigenvalue problem.

When L is chosen such that the Hankel matrices are rectangular rather than square, the problem is instead solved using a pseudo-inverse, leading to a generalized eigenvalue problem

$$Y_0^+ Y_1 v_i = z_i v_i\,, \tag{A.10}$$

where v_i are some eigenvectors to the square matrix $Y_0^+ Y_1$, and the superscript $+$ represents the Moor-Penrose pseudo-inverse [62].

Declaration of using generative AI tools

B

Declaration of using generative AI tools (for students)

At the University of Copenhagen, we do our work with ***responsibility*** *and* ***respect for society, cultural heritage, the environment and people*** *around us.*
Integrity, honesty *and* ***transparency*** *are prerequisites for academic work. We expect exam performances to reflect the* ***student's own learning and independent work****. Academic work is always based on other people's insights, knowledge and contributions, but always with thorough* ***recognition, respect*** *and* ***crediting*** *of this work. This also applies when using generative artificial intelligence.*

Guidelines

Use of generative AI in exams

According to the University's rules for using tools based on generative AI (GAI), you must be transparent about your use of the technology, for example in your methodology section and/or by filling in and submitting the declaration template below as an appendix to your exam papers. When you fill in the declaration, it is important that the reader gets a clear picture of whether and how generative AI has contributed to the final product.

If the template has been chosen as the preferred means of declaration in your course, you must also use it when you have *not* used GAI tools as an aid. In this case, the only thing you need to do is tick the box stating that you have not used generative AI, leaving the rest blank.
By declaring your use of GAI tools, you avoid issues in relation to the rules on exam cheating.

On courses where the use of GAI has been an integrated part of the content, reflection and critical assessment of using GAI may also be included in your exam paper's methodology section. If you are unsure of whether this is the case on your course, you can ask your lecturer or supervisor.

If GAI is the object of your exam paper, its role will appear from your research questions, methodology description, analysis and conclusion. If you also use GAI as an aid in the process, you need to declare it separately.

Points of attention:

- If GAI is a permitted aid on your course, you can use it for dialogue and sparring when writing your exam paper, but you are **not** allowed to let GAI write your paper, even if all aids are permitted.
- If you include GAI material as a source (directly or edited) in your exam paper, the same requirements apply for using quotation marks and source referencing as with all other sources. Otherwise, it will be a case of plagiarism.
- Never feed an AI tool with data that are personally identifiable, protected by copyright or confidential.
- Always remember to check the current rules and guidelines for using GAI at UCPH.
- Read the course description carefully. It's important that you know which aids are permitted on your course. There may be additional documentation requirements, for example that you must describe your key prompts and any source material (what context you have given, what you have fed into the tool, what you have asked the tool to do), describe the output (what responses did the tool give you?), describe the process, for example history and iterations (if you have written back and forth with the tool several times to get a useful output).
- If in doubt, talk to your lecturer or supervisor.

Declaration of using generative AI tools (for students)

☒ **I/we have used generative AI as an aid/tool** *(please tick)*

☐ **I/we have <u>NOT</u> used generative AI as an aid/tool** *(please tick)*

If generative AI is permitted in the exam, but you haven't used it in your exam paper, you just need to tick the box stating that you have not used GAI. You don't have to fill in the rest.

List which GAI tools you have used and include the link to the platform (if possible):

Github Copilot [https://github.com/copilot]
(I use two different here, since I don't pay for them, so I only have limited access.)
Claude [https://claude.ai/]
ChatGPT [https://chatgpt.com/]

Example: [Copilot with enterprise data protection (UCPH license), https://copilot.microsoft.com]

Describe how generative AI has been used in the exam paper:

1) *Purpose (what did you use the tool for?)*
2) *Work phase (when in the process did you use GAI?)*
3) *What did you do with the output? (including any editing of or continued work on the output)*

In this thesis GAI was used for four things. 1) At the start of the project I used GAI to get an overview of the literature, using it almost as a better search engine. 2) And at the end of me writing my thesis, I checked spelling and gramma mistakes. 3) Since GAI, more often then not, hallucinating answers, I always make sure to have search capabilities on, such that I at the end of my prompt always can put "After your answer give me a list of references where all of the information you have given me is located." Then I double check the information it gives me by reading the references. 4) Finally, when I write code, and get errors, I use GAI to figure out what error messages mean, such that I do not have to spend time looking for the specific place in the code that is causing the problem.

Please note: Content generated by GAI that is used as a source in the paper requires correct use of quotation marks and source referencing. Read the guidelines from Copenhagen University Library at KUnet.